Ultrasonic and seismic constraints on crystallographic preferred orientations of the Priestley Glacier shear margin, Antarctica

Franz Lutz[1], David J. Prior[1], Holly Still[2], M. Hamish Bowman[1], Bia Boucinhas[3], Lisa Craw[4], Sheng Fan[1], Daeyeong Kim[5], Robert Mulvaney[6], Rilee E. Thomas[1], and Christina L. Hulbe[2]

[1]Department of Geology, University of Otago, Dunedin, New Zealand
[2]School of Surveying, University of Otago, Dunedin, New Zealand
[3]Antarctica New Zealand, Christchurch, New Zealand
[4]Institute for Marine and Antarctic Sciences, University of Tasmania, Hobart, TAS, Australia
[5]Division of Earth Sciences, Korea Polar Research Institute, Incheon, Republic of Korea
[6]British Antarctic Survey, Natural Environment Research Council, Cambridge, United Kingdom

Correspondence: Franz Lutz (franz.lutz@otago.ac.nz)

Abstract. Crystallographic preferred orientations (CPOs) are particularly important in controlling the mechanical properties of glacial shear margins. Logistical and safety considerations often make direct sampling of shear margins difficult and geophysical measurements are commonly used to constrain the CPOs. We present here the first direct comparison of seismic and ultrasonic data with measured CPOs in a polar shear margin. The measured CPO from ice samples from a 58 m deep borehole in the left lateral shear margin of the Priestley Glacier, Antarctica, is dominated by horizontal c-axes aligned sub-perpendicular to flow. A vertical-seismic-profile experiment with hammer shots up to 50 m away from the borehole, in four different azimuthal directions, shows velocity anisotropy of both P-waves and S-waves. Matching P-wave data to the anisotropy corresponding to CPO models defined by horizontally aligned c-axes gives two possible solutions for c-axis azimuth, one of which matches the c-axis measurements. If both P-wave and S-wave data are used, there is one best fit for azimuth and intensity of c-axis alignment that matches ~~well~~ the measurements well. Azimuthal P-wave and S-wave ultrasonic data recorded in the laboratory on the ice core show clear anisotropy of P-wave and S-wave velocities in the horizontal plane that matches that predicted from the CPO of the samples. With ~~good~~ quality data, azimuthal increments of 30° or less will constrain well the orientation and intensity of c-axis alignment. Our experiments provide a good framework for planning seismic surveys aimed at constraining the anisotropy of shear margins.

1 Introduction

Ice streams and glaciers ~~form~~are localised regions of high ice flow velocity inside otherwise mostly stationary ice masses of Antarctica and Greenland (Truffer and Echelmeyer, 2003) and play a key role in the mass balance of polar ice masses. ~~As result of high flow velocities~~As a result of high-velocity flow, the margins of these streaming ice bodies undergo ~~large~~ strain as they are in contact with stationary ice or rock. Crystallographic preferred orientation (CPO) patterns observed inside glacier margins ~~have been found to~~ indicate a very high degree of crystal alignment in the horizontal direction (Jackson and Kamb, 1997; Monz et al., 2021; Gerbi et al., 2021; Thomas et al., 2021). These results are consistent with observations from shear deformation

experiments of ice where c-axis maxima are always aligned perpendicular to the shear plane (Bouchez and Duval, 1982; Qi et al., 2019; Journaux et al., 2019).

The presence of a CPO results in anisotropic mechanical properties and so influences the viscous behaviour of ice significantly (Azuma and Goto-Azuma, 1996; Budd et al., 2013; Faria et al., 2014; Hudleston, 2015). Shear margins of glaciers ~~are therefore expected to~~therefore can affect the character of ice flow in ice streams due to their distinct mechanical properties (Minchew et al., 2018; Hruby et al., 2020; Drews et al., 2021). The advection of the shear margins during the flow of ice from land to sea can result in bands of strongly deformed ice that transect ice shelves (LeDoux et al., 2017) and can potentially affect the stability of ice shelves. Modelling suggests that remnant CPO resultant in shear margins can be present 10000 years after advection downstream (Lilien et al., 2021).

A better understanding of CPO patterns in glacier shear margins is therefore highly desirable to accurately ~~represent~~determine their mechanical properties. Ice core drilling, the primary direct information source for CPO, is however rarely performed on fast-flowing ice because of difficulties in access and on site safety. Geophysical studies, e.g. seismic (Bentley, 1971; Blankenship and Bentley, 1987; Picotti et al., 2015; Vélez et al., 2016) or radar (Matsuoka et al., 2003; Jordan et al., 2020; Ershadi et al., 2021) surveys provide an alternative way of constraining bulk CPO. Ideally, geophysical work should be combined with drilling, to recover ice samples for microstructure analysis, and so enable a cross-calibration of CPO constraints.

A continuous ice core of 58 m length was drilled and recovered in December 2019 and January 2020 (Thomas et al., 2021) in a lateral shear margin of the Priestley Glacier, located in Victoria Land, Antarctica, see Figure 1(a). There is no firn layer on the glacier, however a snow cover of approximately 0.4 m was present at the time of drilling. At the site the glacier is ~ 1000 m thick and 8 km wide (Frezzotti et al., 2000). Ice flow velocities are measured to increase from ~ 45 m/year close to the glacier margin to ~ 130 m/year towards the center (Mouginot et al., 2019; Thomas et al., 2021), resulting in strong shear ~~kinematics~~,with shear strain rates at the site calculated to be $6 \cdot 10^{-10} s^{-1}$ (Still et al., 2022; Thomas et al., 2021). Core samples were analysed for CPO using electron backscatter diffraction (EBSD) measurements (Thomas et al., 2021) and a strong horizontal clustering of c-axes was observed throughout the entire length of the core. The core orientation was carefully preserved during drilling, which enabled ~~the placement of CPO orientation relative to the macroscopic ice kinematics.~~azimuthal orientation of the CPO. The horizontal c axis cluster orientation varies between approximately perpendicular to ice flow to 130° clockwise (looking down) of ice flow direction.

After completion of drilling and core retrieval, the open borehole was used to conduct a vertical-seismic-profile (VSP) experiment to constrain seismic properties of the near-surface glacier ice, with a particular focus on seismic anisotropy. To complete the link between seismic anisotropy of the ice volume around the borehole and CPO measurements from the core, multiazimuthal ultrasonic velocity measurements (Langway et al., 1988; Hellmann et al., 2021) were made on core samples in the laboratory.

The anisotropy of single ice crystals displays hexagonal symmetry, i.e. wave velocity is only dependent on the angle between propagation direction and c-axis, with the fast P-wave propagation direction parallel to the c-axis (Gammon et al., 1983). Seismic P- and S-wave velocities at different propagation angles relative to the c-axis of a single crystal are shown in Figure 2.

This study presents the first of its kind to explicitly study the very specific Horizontal_Cluster_CPO type observed in shear margins with seismic methods. Analyses of seismic, ultrasonic and measured CPO datasets are combined to assess the potential of active source seismic surveys for the constraint of shear margin anisotropy.

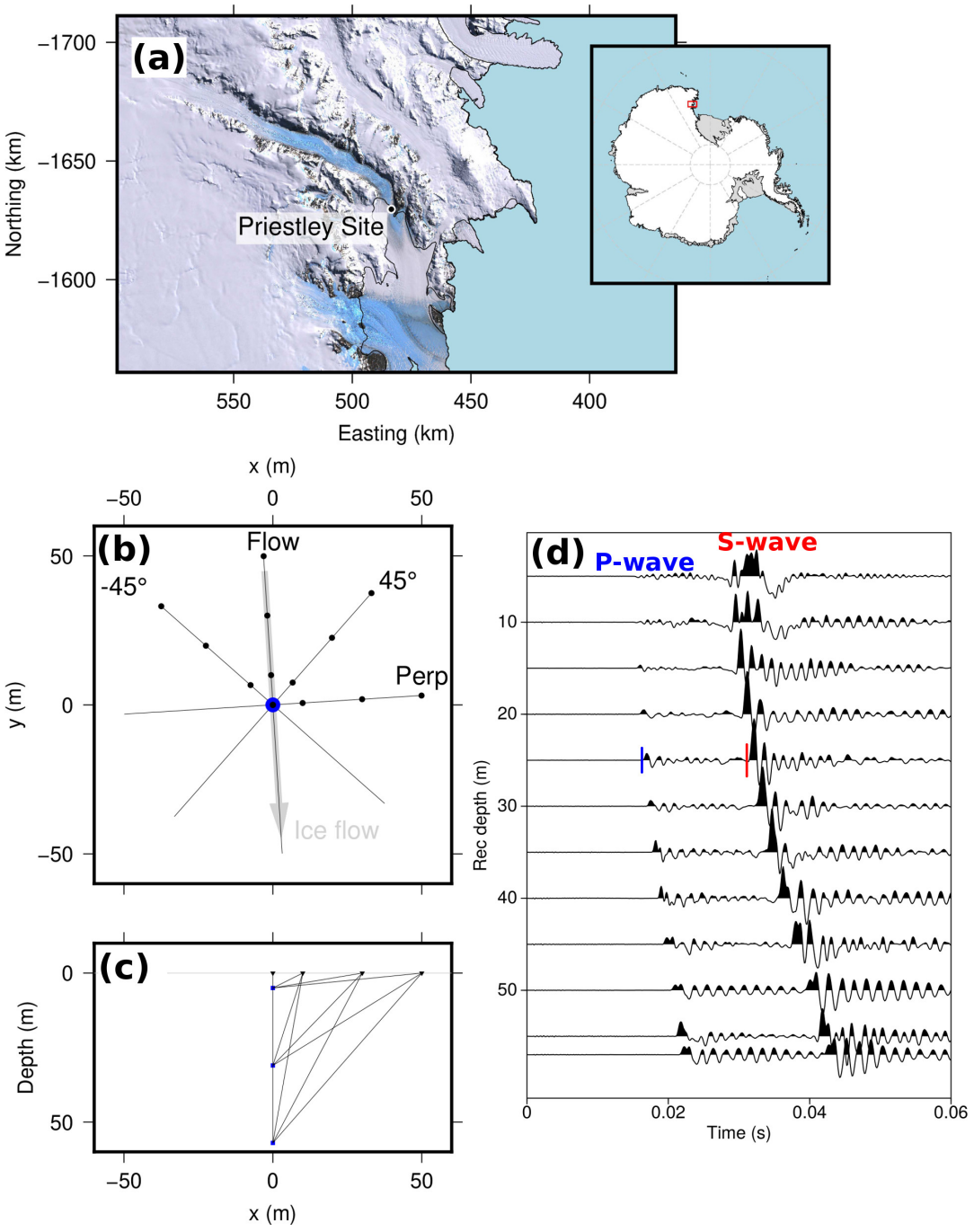

Figure 1. (a) Regional map of the Priestley Glacier site. Coordinates are given by the polar stereographic projection with latitude of true scale at -71°S. Landsat Image courtesy of USGS. (b) Map view illustration of VSP geometry. Black markers show shot point locations, the borehole location is shown in blue. (c) Cross-section illustration of VSP geometry showing the surface shotpoints in black and three borehole seismometer positions in blue. (d) Vertical component traces of borehole seismometer for shots at 50 m offset along the 45°-profile. Example P- and S-wave arrival time picks are shown at 25 m depth as red vertical lines.

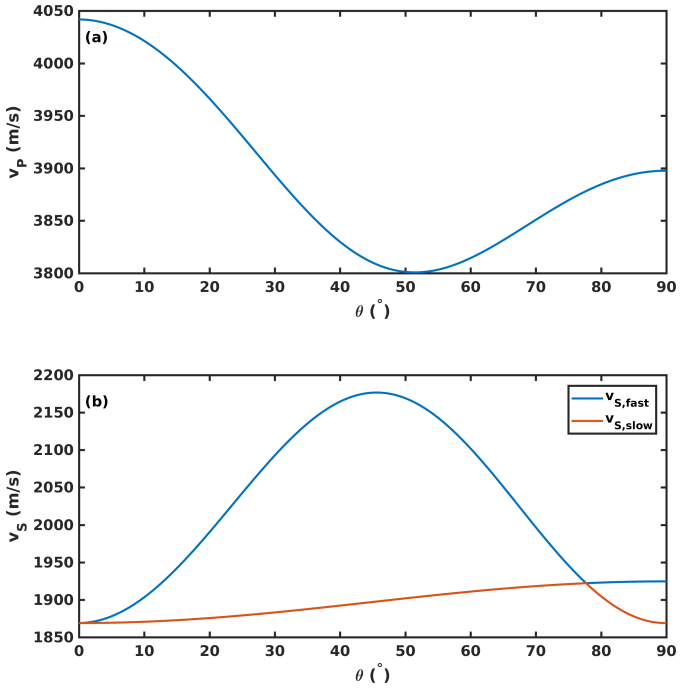

Figure 2. Seismic phase velocities for a single crystal in dependence of angle θ to the c-axis, calculated with values for the elastic constants from adiabatic single crystal artificial water ice at $-16\,^{\circ}$C from Gammon et al. (1983) using the MTEX toolbox (Mainprice et al., 2011). (a) P-wave velocity v_P (b) S-wave velocities v_S

2 ~~Seismic anisotropy informed by~~Analysis of a vertical-seismic-profile ~~shooting~~

2.1 Data acquisition

A VSP dataset was recorded at the Priestley drill site using a three-component borehole seismometer (built by ESS Earth Sciences, Victoria, Australia) with a pneumatic clamping system which was installed in depths z between 5 m and 57 m below the glacier surface. The suspension cable, to the centre of the seismometer, remained close to the centre of the hole at the surface for all seismometer depths indicating true verticality of the borehole. Signals from a hammer-and-plate source were recorded using a Geometrics Geode for a walkaway-VSP geometry along four profiles with different azimuths, where shots were placed at offsets x of 0 m ("Zero-offset" geometry), 10 m, 30 m and 50 m from the top of the borehole. Profile names ("Flow", "Perp", "45", "-45") indicate their orientation relative to the glacier flow direction (see Table 1). The survey geometry is illustrated in Figure 1(b). The depth increments of the borehole seismometer along the four profiles are shown in Table 1.

Table 1. Multi-azimuth VSP survey parameters.

Shot profile orientation (Profile name)	Seismometer depth increment (m)
Zero-offset	1
Flow-parallel ("Flow")	1
Flow-perpendicular ("Perp")	2.5
45° to flow ("45")	5
$-45°$ to flow ("-45")	5

Data recording for each shot in the field was initiated by a Geometrics switch trigger taped to the sledgehammer handle. Quality control of traces in the field found that this trigger type produces inconsistent zerotimes and the recorded signal from surface geophones collocated at the shot points were used to define shot times. The Geode was set to record 100 ms before the hammer switch trigger signal to allow manual picking of the first-arrival time on the shotpoint surface geophone, which corresponds to the time of hammer impact. Total recording length was 2 s with a sampling ~~interval of 0.125 ms~~rate of 8000 Hz. Shot and geophone locations were cleared of all snow cover to ensure direct contact of source and receivers to the hard ice surface. Several repeat shots were recorded at all shot points along a given profile for one seismometer depth before the instrument was lowered to the next depth. After all shots for all seismometer depths were completed for a profile, surface geophones were moved to the next profile position.

Polarisation patterns indicate a ringing effect of the pneumatic borehole seismometer, where phase arrivals are followed by a tail of mono-frequent oscillations (see traces in Figure 1(d)). The oscillations are distributed along all three seismometer components ~~and therefore it was found that a~~, even after separation of P- and S-wave signals through component rotation into ray coordinates (Wüstefeld et al., 2010) ~~is not achievable in the VSP dataset~~. This noise in the phase arrival signals ~~precludes~~impedes investigating polarisation patterns, such as S-wave splitting, as a constraint on seismic anisotropy (Lutz et al., 2020).

2.2 Multi-azimuth VSP traveltimes

P- and S-wave first arrival signals were recorded with high signal-to-noise ratio and phase arrival times can be clearly identified. Picking of seismic phase arrivals is performed manually for each shot to determine traveltimes: one first arrival pick is made on the surface geophone trace at the shot location in addition to picks of P- and S-wave arrivals on the borehole seismometer traces. The P- and S-wave traveltime t is then calculated as the difference between the picked arrival time on the borehole seismometer and the picked source time on the surface geophone.

Observed P-wave traveltimes along the seismic profiles are presented in Figure 3(a)-(d). The zero-offset P-wave traveltimes in Figure 3(a) can be approximated by a constant velocity model ($v_P = 3850$ m/s, solid line). This highlights that there is little velocity variation due to heterogeneity in the shallow glacier ice.

Differences in traveltimes between the profiles become apparent for shots at offsets ≥ 30 m and below seismometer depths of ~ 25 m. The Flow- and $-45°$-profiles show consistently earlier P-wave arrivals than the Perp- and $45°$-profiles.

Observed S-wave traveltimes are presented in Figure 3(f)-(h) for shots from the four wakaway VSP profiles. Signal-to-noise ratios from zero-offset shots were found to be insufficient to allow picking of S-wave arrivals, likely a consequence of the radiation patters of a plate seismic source which produces no S-wave energy in the vertical direction. The first indication of S-wave arrivals was picked consistently, traveltimes are therefore interpreted to be representative of the fast S-wave velocity v_{S1} ~~and will be consistently referred to as fast S-wave properties throughout this study~~. Systematic traveltime differences between profiles are observed particularly for shots from 50 m offset, where the $-45°$-profile shows the earliest arrival times over almost the entire depth range. Only for seismometer depths below 50 m are traveltimes from the Perp-profile measured at the same time~~s~~ or earlier than traveltimes from along the $-45°$-profile. The Flow- and $45°$-profiles show similar traveltimes that are ~~registered later~~slower than the traveltimes along the other profiles.

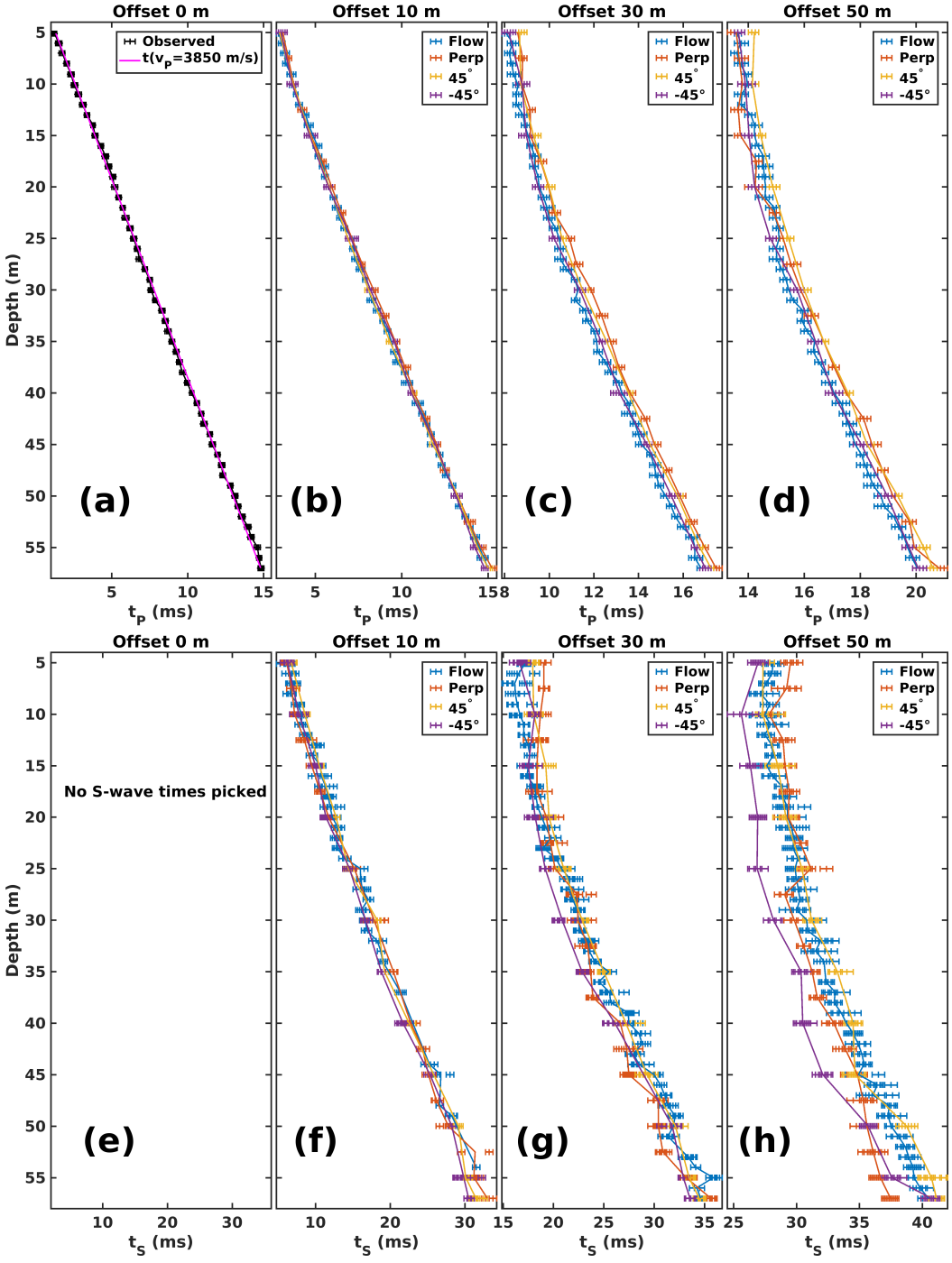

Figure 3. VSP traveltimes observed along the four shot profiles. (a) P-wave traveltimes for shots from 0 m offset. (b) P-wave traveltimes for shots from 10 m offset. (c) P-wave traveltimes for shots from 30 m offset. (d) P-wave traveltimes for shots from 50 m offset. (e) No S-wave traveltimes were picked from 0 m offset shots due to poor signal-to-noise-ratio. (f) S-wave traveltimes for shots from 10 m offset. (g) S-wave traveltimes for shots from 30 m offset. (h) S-wave traveltimes for shots from 50 m offset.

2.3 Velocity ~~anisotropy~~calculation

Seismic velocities are calculated ~~using Equation (1)~~ from the presented traveltimes for different depths z, offsets x and azimuths in Figure 3~~.~~:

$$v = \frac{\sqrt{x^2 + z^2}}{t} \tag{1}$$

The calculation is based on the assumption of straight raypaths between shot and receiver, which is regarded as valid approximation for a site location on hard ice without snow cover. The seismic waves travel entirely in ice and no large velocity gradients that could result in significant raypath bending are therefore expected (Gusmeroli et al., 2013). The zero-offset traveltimes in Figure 3(a) exhibit no apparent indications of velocity gradients since they can be approximated by a constant vertical P-wave velocity. We therefore assume the ice volume sampled by the VSP experiment to be characterised by a homogeneous, constant-CPO layer. The incidence angle θ from the vertical direction is defined ~~by Equation (2).~~as:

$$\theta = \arctan\left(\frac{x}{z}\right) \tag{2}$$

Velocity uncertainties Δv are calculated ~~using Equation (3)~~ from uncertainty estimates for P-wave traveltime $\Delta t_P = 0.125\,\text{ms}$, S-wave traveltime $\Delta t_S = 1\,\text{ms}$, offset $\Delta x = 0.2\,\text{m}$ and depth $\Delta z = 0.1\,\text{m}$. ~~Observations with relative uncertainty $\Delta v/v > 0.05$ are discarded from further analysis. The range of observed velocities along the different shot profiles is presented in Table **??**.~~

$$\Delta v = \frac{x\Delta x + z\Delta z}{t \cdot \sqrt{x^2 + z^2}} + \frac{\Delta t \cdot \sqrt{x^2 + z^2}}{t^2} \tag{3}$$

Observations with relative uncertainty $\Delta v/v > 0.05$ are discarded from further analysis.

3 ~~Seismic anisotropy informed by~~Analysis of ultrasonic experiments

Ultrasonic experiments were performed inside a freezer at temperature $-23 \pm 2\,^{\circ}\mathrm{C}$ on a subset of samples from the continuous ice core. Samples were lathed to the shape of a highly regular cylinder. Traveltime measurements were made perpendicular to the core axis in multiple azimuths to inform ultrasonic velocities in the horizontal direction of the glacier ice. ~~U~~Olympus ultrasonic P- or S-wave transducers were spring loaded against the cylinder surface, on opposing sides of the cylinder (Figure 4(a)+(b)). S-wave transducers were used for excitation and recording of S-waves with polarisations in the vertical (parallel to the long core axis) and horizontal (perpendicular to the long core axis) direction. Coupling of transducers to the ice core samples was ensured through the use of synthetic high-performance low temperature grease.

Traveltime measurements across the ice core were made in azimuthal increments of 10° covering the full core diameter, resulting in $N = 36$ measurements per transducer arrangement and core. A fiducial line that was made in the field to provide geographic reference of the core orientation served as the 0° reference on individual samples. The fiducial line was made perpendicular to the glacier flow direction on the surface (Thomas et al., 2021). New fiducial lines were started wherever a core break could not be fitted together and the relative orientations of the lines reconstructed using the core CPO (Thomas et al., 2021). Measurements are on core sections 003 from a depth of $\sim 2.5\,\mathrm{m}$ (diameter $d = 100.6 \pm 0.3\,\mathrm{mm}$), 007 from a depth of $\sim 6.0\,\mathrm{m}$ (diameter $d = 99.9 \pm 0.3\,\mathrm{mm}$) and 010 from a depth of $\sim 8.5\,\mathrm{m}$ (diameter $d = 100.3 \pm 0.3\,\mathrm{mm}$). The in-situ temperature at the sample depths was observed to be between $\approx -7\,^{\circ}\mathrm{C}$ and $\approx -15\,^{\circ}\mathrm{C}$ (Thomas et al., 2021). Ultrasonic measurements made at these warmer temperatures did not result in any measurable effect on seismic anisotropy. Since warmer temperatures also caused problems with transducer coupling to the ice cores, the initially described freezer temperature setting at $-23 \pm 2\,^{\circ}\mathrm{C}$ was used for the ultrasonic experiments.

The ultrasonic source signal pulse was created by a JSR Ultrasonics DPR300 Pulser unit and shows a dominant frequency $f \approx 1\,\mathrm{MHz}$, resulting in a dominant wavelength of $\lambda \approx 3.8\,\mathrm{mm}$ in the ice. Recording of the source and receiver signal was performed on separate oscilloscope channels by a PicoScope digital oscilloscope with a sampling ~~rate~~interval $t_S = 0.8\,\mathrm{ns}$. Signals were recorded directly by the oscilloscope without the use of amplifiers. The source signal was used to trigger signal recording by exceedance of an amplitude threshold. A signal length of $100\,\mu\mathrm{s}$ after triggering is recorded.

3.1 Processing

At each azimuth 64 individual waveforms were recorded. The mean amplitude and linear trend is removed from these individual traces before they are stacked to increase signal-to-noise ratio. The stacked traces are tapered and filtered with a bandpass filter with corner frequencies $f_1 = 50\,\mathrm{KHz}$ and $f_2 = 5\,\mathrm{MHz}$ and normalised for plotting.

Waveforms recorded on sample ~~sample~~ 007 are shown in Figure 4(c)-(e). The core orientation angle in these plots is relative to the fiducial marker on the core sample. Recorded waveforms using the P-wave transducers are shown in Figure 4(c). A rotational symmetry with periodicity of 180° is present, which confirms a consistent and reliable excitation and recording of P-wave signals for all azimuths around the core.

Waveforms recorded using S-wave transducers set for vertical vibration are shown in Figure 4(d), indicating a clear periodicity of 180° and are predominantly indicative of the slow S-wave velocity v_{S2}.

Waveforms from S-wave transducers set for horizontal vibration are shown in Figure 4(e). Here, four local maxima in velocity are observed for the full range of azimuths. This arrangement of transducers ~~is found to enable~~enables the measurement of fast S-wave velocity v_{S1} at most azimuths.

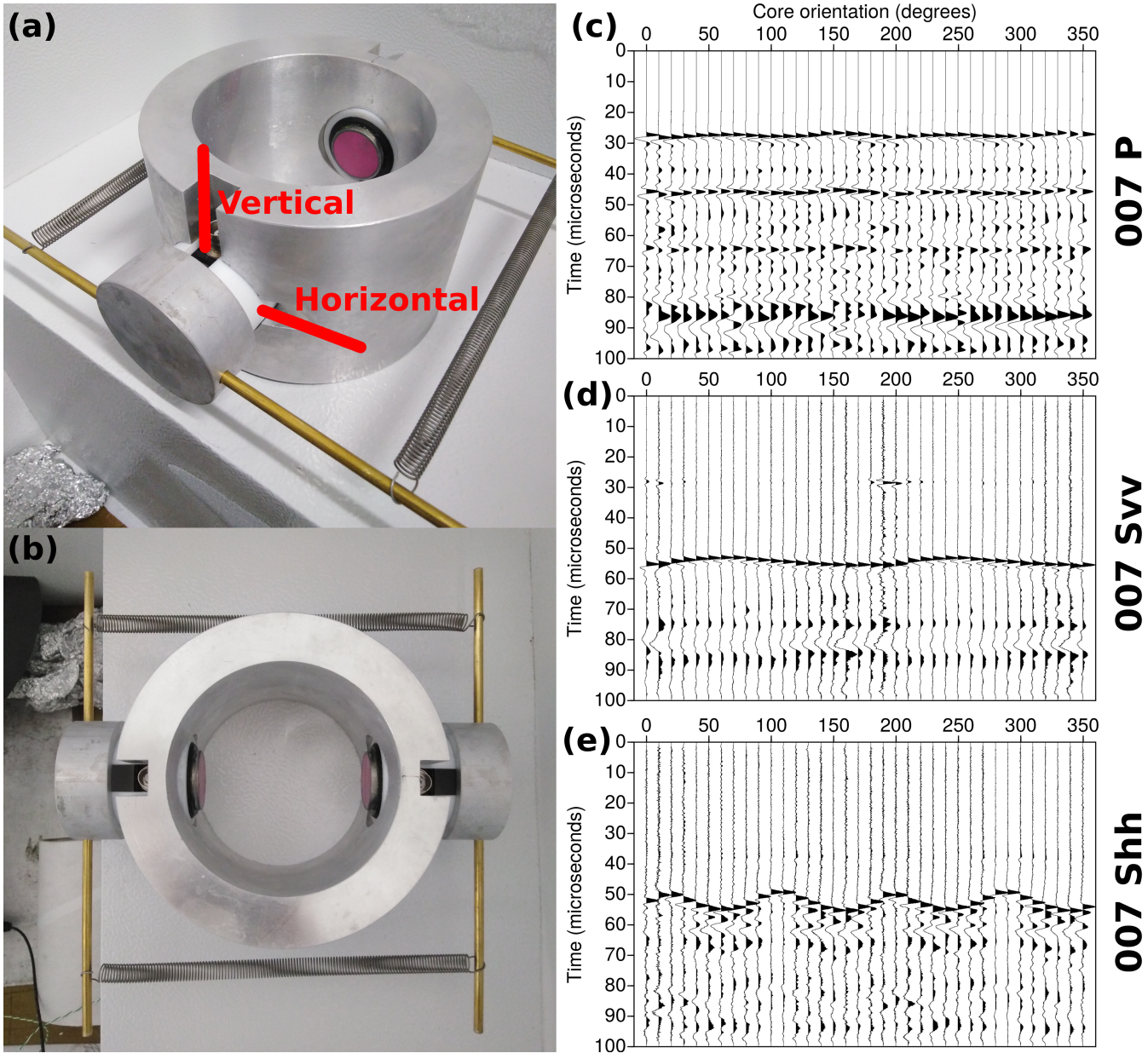

Figure 4. (a) Side view of ultrasonic rig with slots for different transducer orientations highlighted. (b) Map view of ultrasonic rig. Transducers are set for vertical vibration. (c) Multiazimuth signal traces using P-wave transducers on sample 007. (d) Multiazimuth signal traces using S-wave transducers set for vertical vibration on sample 007. (e) Multiazimuth signal traces using S-wave transducers set for horizontal vibration on sample 007.

3.2 P-wave and S-wave ultrasonic velocity results

Arrival times t of the direct P- and S-wave phases are picked by hand on the stacked traces and used to calculate ~~seismic~~ultrasonic velocities $v = d/t$. Successful measurements of v_P, v_{S1} and v_{S2} are made at all azimuths and samples, which constitutes an unprecedented characterisation of ~~seismic~~ultrasonic velocity anisotropy in high detail. Velocity uncertainties are calculated from diameter uncertainty $\Delta d = 0.3$ mm and picking uncertainty $\Delta t = 0.1\,\mu$s.

Ultrasonic P- and S-wave velocities of the three studied core sections are shown in Figure 5(a)-(c). The velocities are presented in the kinematic reference frame, where the angles relative to the fiducial lines on individual samples are transformed to give the orientation relative to glacier flow at the site (Thomas et al., 2021). The azimuth given in the plots presents the angle from the flow-parallel VSP profile in Figure 1(b) in clockwise direction.

The largest P- and S-wave velocities are observed in sample 007, sample 003 shows the lowest velocities and intermediate velocities are measured in sample 010. A variation of seismic velocities with azimuth is present in all samples. Shapes of the velocity curves are very similar for the three individual samples, however the observed velocities of 003 are shifted by an angle of $\approx 20°$ relative to the curves of 007/010.

Ultrasonic v_P measurements were also made along the core axis, sampling the vertical direction also at $-23 \pm 2\,°$C. Sample velocities of $v_{P,vert,003} = 3838 \pm 20$ m/s, $v_{P,vert,007} = 3822 \pm 15$ m/s and $v_{P,vert,010} = 3842 \pm 18$ m/s again highlight near constant velocity with depth implicit in the zero-offset VSP P-wave traveltimes (Figure 3(a)). The range of vertical v_P is shown in Figure 5(a). The observation that vertical v_P is faster than horizontal v_P for most azimuths is inconsistent with the expected velocities for a Horizontal-Cluster-CPO and no definite explanation for this observation is available at this point. Potential additional influences on velocities could be given by populations of "oddly" oriented grains (Thomas et al., 2021) that show orientations in the horizontal plane but outside of the c-axis cluster. They could therefore reduce the maximum v_P along the cluster axis, but not affect v_P in the vertical direction. Anisotropy related to preferred bubble shape or aligned cracks, both observed in the uppermost ≈ 10 m of the ice core (Thomas et al., 2021), could also play a role.

An attempted measurement of v_S in the vertical direction failed, because no clear ultrasonic S-wave signals that allowed traveltime picking could be recorded in this geometry.

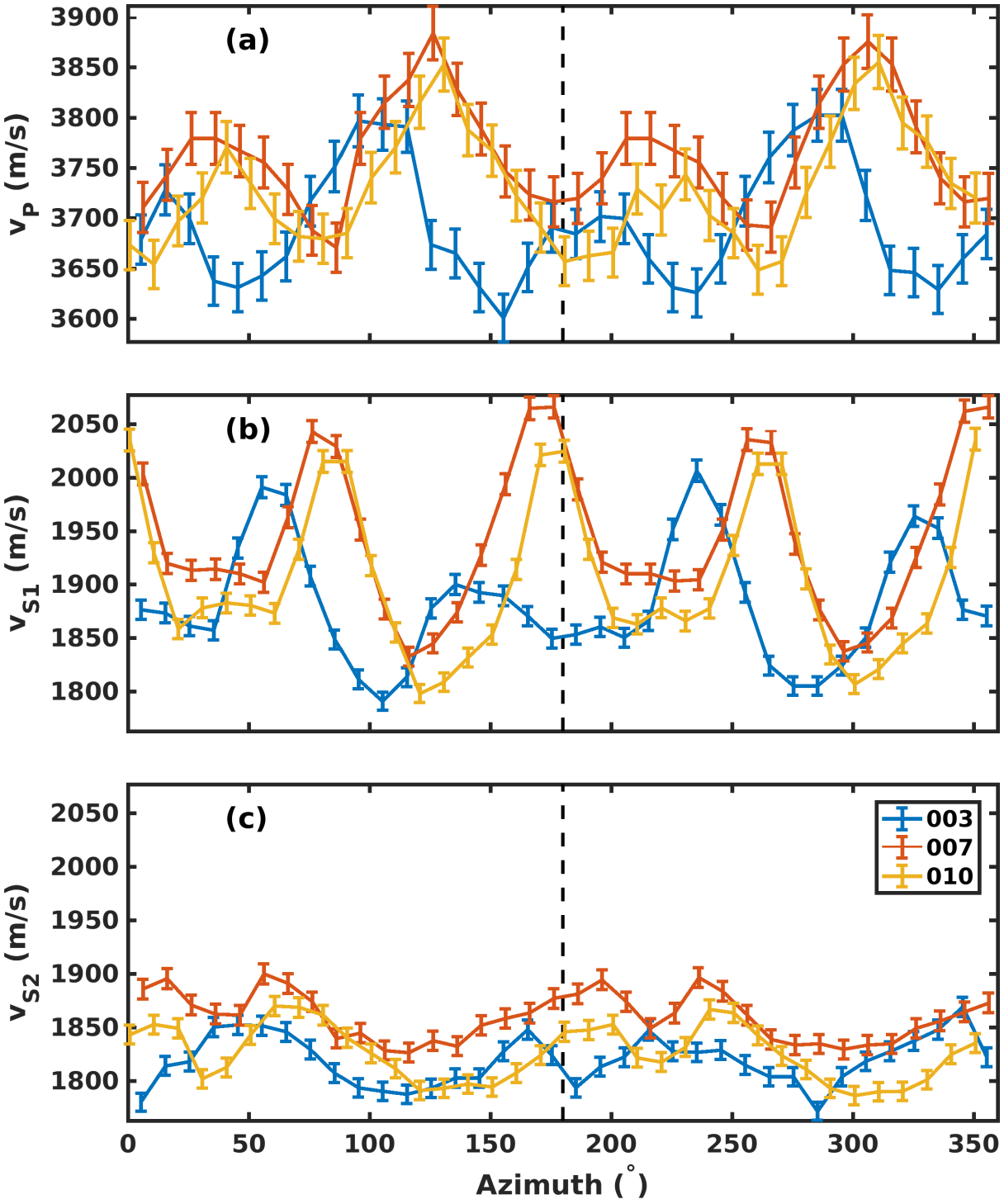

Figure 5. Ultrasonic multiazimuth velocities for different core sections relative to the macroscopic glacier flow direction (0°). (a) P-wave velocity v_P. The gray-shaded box shows the range of measured vertical ultrasonic v_P. (b) Fast S-wave velocity v_{S1}. (c) Slow S-wave velocity v_{S2}.

4 CPO modelling

The observed high degree of seismic anisotropy in VSP seismic and multiazimuth ultrasonic data is consistent with the observation of strong CPO in the retrieved core samples from the site. EBSD measurements on core samples constrain the CPO to be characterised by a strong clustering of c-axes in the horizontal plane (Thomas et al., 2021). The availability of constraints from sample microscopic analysis and geophysical data at the Priestley Glacier site is therefore ~~very~~ suitable for a calibration of seismic properties to the known CPO. The observed P- and S-wave velocity anisotropies from VSP and multiazimuth ultrasonic observations are compared to models of polycrystal elasticity connected to CPOs comprising horizontally clustered c-axes. In general, when interpreting geophysical data no CPO constraints are available and a range of different CPO geometries has to be tested to match observations (Diez and Eisen, 2015; Maurel et al., 2015; Lutz et al., 2020). We skip this step and focus entirely on the influence of survey geometry and suitability of P- and S-wave velocity information for constraining ice CPO. ~~The workflow of matching observed seismic properties to synthetic properties from CPO forward models is a modification of the approach introduced in Lutz et al. (2020).~~

4.1 Horizontal-Cluster-CPO

CPO models are created using the MTEX toolbox for Matlab (Mainprice et al., 2011) consisting of 1000 clustered c-axes with cluster symmetry axis in the horizontal direction. A geometrical description of this Horizontal-Cluster-CPO forward model can be given by a ~~cone~~diffused cluster with symmetry axis in the horizontal plane that encompasses the clustered c-axes. The model parameters of this ~~cone~~cluster geometry are defined by the azimuth φ of the ~~cone symmetry axis~~center of the cluster and the ~~cone opening~~cluster width angle α. An illustration of this CPO type is presented in Figure 6 in an upper-hemisphere stereographic projection.

Seismic properties of individual crystals are characterised by the elasticity tensor C in Equation (4) of synthetic ice at $-16\,^{\circ}\mathrm{C}$ by Gammon et al. (1983) and density $\rho = 919.1\,\mathrm{kg/m^3}$. For any given set of CPO model parameters φ and α, synthetic seismic velocities associated with the CPO are calculated after forming the Voigt-Reuss-Hill-average elastic properties (Hill, 1952; Mainprice, 2007).

$$C = \begin{bmatrix} 13.913 & 7.026 & 5.801 & 0 & 0 & 0 \\ 7.026 & 13.913 & 5.801 & 0 & 0 & 0 \\ 5.801 & 5.801 & 15.059 & 0 & 0 & 0 \\ 0 & 0 & 0 & 3.011 & 0 & 0 \\ 0 & 0 & 0 & 0 & 3.011 & 0 \\ 0 & 0 & 0 & 0 & 0 & 3.4435 \end{bmatrix} \text{GPa} \tag{4}$$

Model parameters φ and α are systematically varied in regular step sizes and all combinations within the individual parameter ranges presented in Table 2 are explored. Synthetic seismic properties are compared to observations for each model realisation.

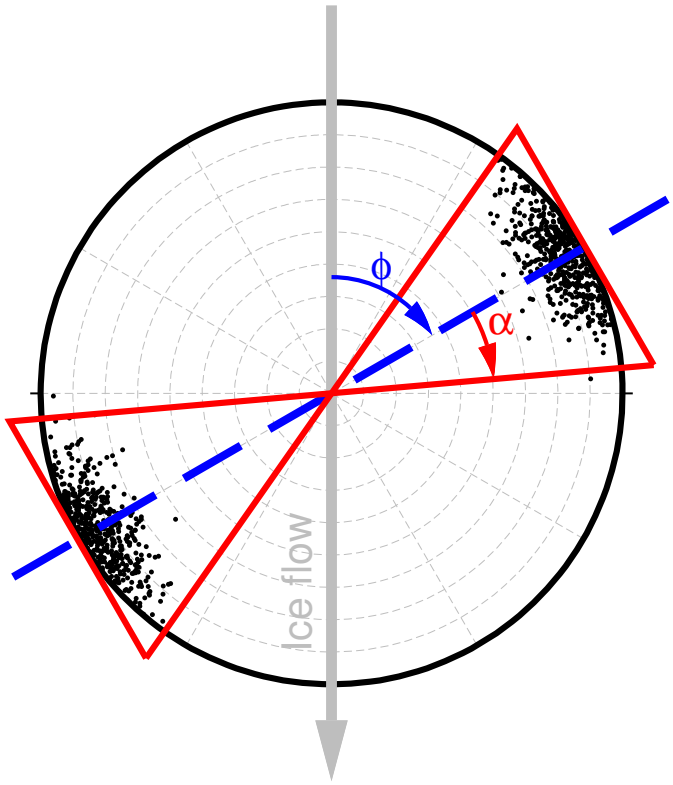

Figure 6. Upper-hemisphere stereographic projection of an example Horizontal-Cluster-CPO model with illustration of model parameters: Cluster orientation φ and opening angle α.

Table 2. Horizontal-Cluster-CPO model parameters.

Parameter	Start value	End value	Step size
Cluster orientation φ	0°	180°	5°
Opening angle α	0.1°	40.1°	1°

4.2 Model misfit calculation

The ability of a CPO model to explain measured seismic anisotropy is assessed by introduction of a misfit between synthetic forward modelled seismic properties and observations. We found that CPO predicted seismic velocities are consistently faster than observed velocities, an effect which can be attributed to the absence of grain boundary effects (Sayers, 2018) or air bubbles (Hellmann et al., 2021) in synthetic CPOs. The elasticity tensor by Gammon et al. (1983) was derived using oscillations in GHz frequencies, therefore dispersion is another potential factor to introduce differences between modelled and observed seismic

or ultrasonic velocities with Hz to kHz frequencies. ~~Because of these effects,~~A normalisation is introduced to address these described effects on absolute velocities and we focus entirely on modelled and observed anisotropic velocity variations rather than absolute velocities, studying the variation of velocities ~~$v(\vartheta)$ along different angles ϑ~~ relative to the mean velocity ~~along all observation angles~~. This definition of seismic anisotropy δv is given in Equation (5), where $\bar{v}$ is the mean wave velocity of all observations.

$$\delta v = \left(\frac{v}{\bar{v}} - 1\right) \cdot 100 \tag{5}$$

We consider the elasticity data from Gammon et al. (1983) to provide high accuracy of relative velocity variation. Therefore we have chosen to rely upon these data and no other published elasticities of ice are investigated to match the observed anisotropy, such as done in previous studies which compared absolute measured and synthetic velocities (Diez et al., 2015; Picotti et al., 2015). A misfit ~~χ~~χ_{raw} is calculated by Equation (7) between measured (δv) and synthetic (δv_M) velocity variations. N is the number of velocity observations.

$$\chi_{raw}(v) = \sqrt{\frac{1}{N}\sum_{i=1}^{N}(\delta v_i - \delta v_{M,i})^2} \tag{6}$$

Misfits ~~$\chi(v)$~~$\chi_{raw}(v)$ are calculated individually for the v_P, v_{S1} and v_{S2} observations and all synthetic CPO models. The $\chi(v_P)$, $\chi(v_{S1})$ and $\chi(v_{S2})$ misfits are then ~~individually normalised~~calculated through division by the largest misfit of all models.

$$\chi(v) = \chi_{raw}(v)/\max(\chi_{raw}(v)) \tag{7}$$

In addition, misfit averages are defined as:

$$\chi(v_P) + \chi(v_{S1}) = \frac{1}{2}\left(\frac{\chi_{raw}(v_P)}{\max(\chi_{raw}(v_P))} + \frac{\chi_{raw}(v_{S1})}{\max(\chi_{raw}(v_{S1}))}\right) \tag{8}$$

$$\chi(v_P) + \chi(v_{S1}) + \chi(v_{S2}) = \frac{1}{3}\left(\frac{\chi_{raw}(v_P)}{\max(\chi_{raw}(v_P))} + \frac{\chi_{raw}(v_{S1})}{\max(\chi_{raw}(v_{S1}))} + \frac{\chi_{raw}(v_{S2})}{\max(\chi_{raw}(v_{S2}))}\right) \tag{9}$$

4.3 CPO model fit using VSP velocities

The model misfit of the VSP data is calculated using $N_P = 1354$ and $N_{S1} = 1036$ velocity observations. Figure 7(a) shows the ~~normalised misfit values for all models using P-wave velocities~~model misfits based on P-wave velocities $\chi(v_P)$. The best-fitting model is indicated by the red dot ~~and t~~.This model CPO is shown in Figure 7(d). Figures 7(b) and 7(e) show S-wave misfits $\chi(v_{S1})$ and the corresponding best-fitting CPO model. The ~~sum of misfits $\chi(v_P)$ and $\chi(v_{S1})$~~misfit average $\chi(v_P) + \chi(v_{S1}$ is presented in 7(c), with its best-fitting CPO model presented in Figure 7(f). Parameters of the best-fitting CPO models ~~using the~~based on VSP observations are provided in Table 3. Parameter uncertainties are taken from the range of models that produce the minimum 1% of misfits.

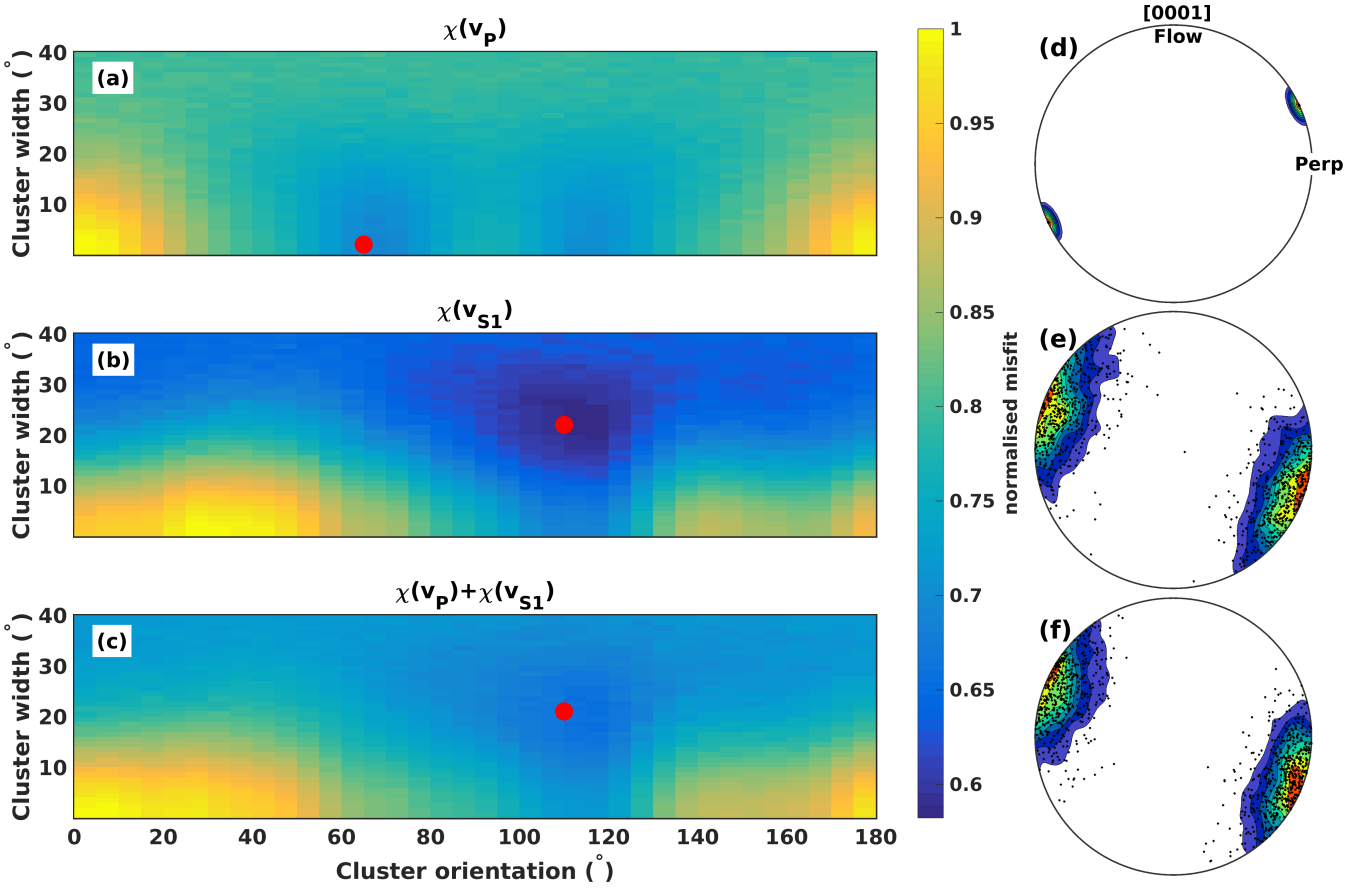

Figure 7. (a) Misfit surface considering only P-wave velocities. (b) Misfit surface considering only S-wave velocities. (c) Misfit surface considering P- and S-wave velocities. (d) Best-fitting CPO model result considering only P-wave velocities. Labels indicate the orientation of the "Flow" and "Perp" profile shots in the VSP survey (compare Figure 1(b)). (e) Best-fitting CPO model result considering only S-wave velocities. (f) Best-fitting CPO model result considering P- and S-wave velocities.

Table 3. Best-fitting CPO model parameters and uncertainties informed by VSP data.

Misfit type	Cluster orientation φ (°)	Cluster width α (°)	Misfit [1% Misfit]
$\chi(v_P)$	65^{+5}_{-0}	2.1^{+7}_{-2}	0.69 [0.70]
$\chi(v_{S1})$	110^{+5}_{-5}	22.1^{+4}_{-3}	0.58 [0.59]
$\sum\chi$	115^{+0}_{-5}	18.1^{+6}_{-2}	0.66 [0.66]

Figure 8 shows the observed P-wave anisotropy δv_P (symbols) along the four survey profiles together with predicted anisotropy from the ~~three best-fitting~~ CPO models presented in Table 3 (dashed lines) ~~in Figure 7~~. The observed variation of

velocities with incidence angle is consistent across all seismometer depths, strengthening the assumption that no change in CPO with depth is present within the investigated ice volume. Modelled anisotropies ~~(dashed lines)~~ generally match observations ~~(symbols)~~ within uncertainties along the Flow-, Perp- and $-45°$ profiles. It is notable that the three different models exhibit very similar seismic properties along these profiles, although the CPO model informed by $\chi(v_P)$ in Figure 7(d) shows a fundamentally different geometry than the other CPO models ~~informed by $\chi(v_{S1})$ or $\chi(v_P)+\chi(v_{S1})$~~shown in Figures 7(e) + and (f). The $-45°$ profile shows a larger difference between the models with a steady decrease in δv_P predicted by the models informed by $\chi(v_{S1})$ and $\chi(v_P)+\chi(v_{S1})$, while the $\chi(v_P)$ CPO model suggests a decrease of δv_P to incidence angles of $\sim 40°$, followed by increasing δv_P towards larger incidence angles. The difference between data and models is largest along this profile, however the observed δv_P support the steady decrease of P-wave velocity between vertical ($0°$) and horizontal incidence ($90°$) that is suggested by the $\chi(v_{S1})$ and $\chi(v_P)+\chi(v_{S1})$ CPO models.

Fast S-wave anisotropy δv_{S1} observations are shown in Figure 9 alongside the modelled anisotropy. Measured velocities exhibit a variation with incidence angle which is consistent across all seismometer depths. Again, observations and models are all in general agreement on the Flow and Perp profile, albeit an observed decrease in δv_{S1} on the Perp profile for incidence angles $\geq 60°$ which is not satisfyingly matched by any model. The most significant differences are seen along the $45°$ and $-45°$ profile, here only the models informed by $\chi(v_{S1})$ and $\chi(v_P)+\chi(v_{S1})$ match observations, while the model informed by $\chi(v_P)$ is strongly mismatched.

~~The acquisition geometry of the VSP survey has to be regarded critically, since two profiles (Flow and Perp) show signals of anisotropy that can ambiguously be explained by CPO models that have fundamentally different cluster geometries. Only the incorporation of diagonal profiles and especially the combination of P- and S-wave information is able to rule out the unrealistic CPO model informed by $\chi(v_P)$.~~

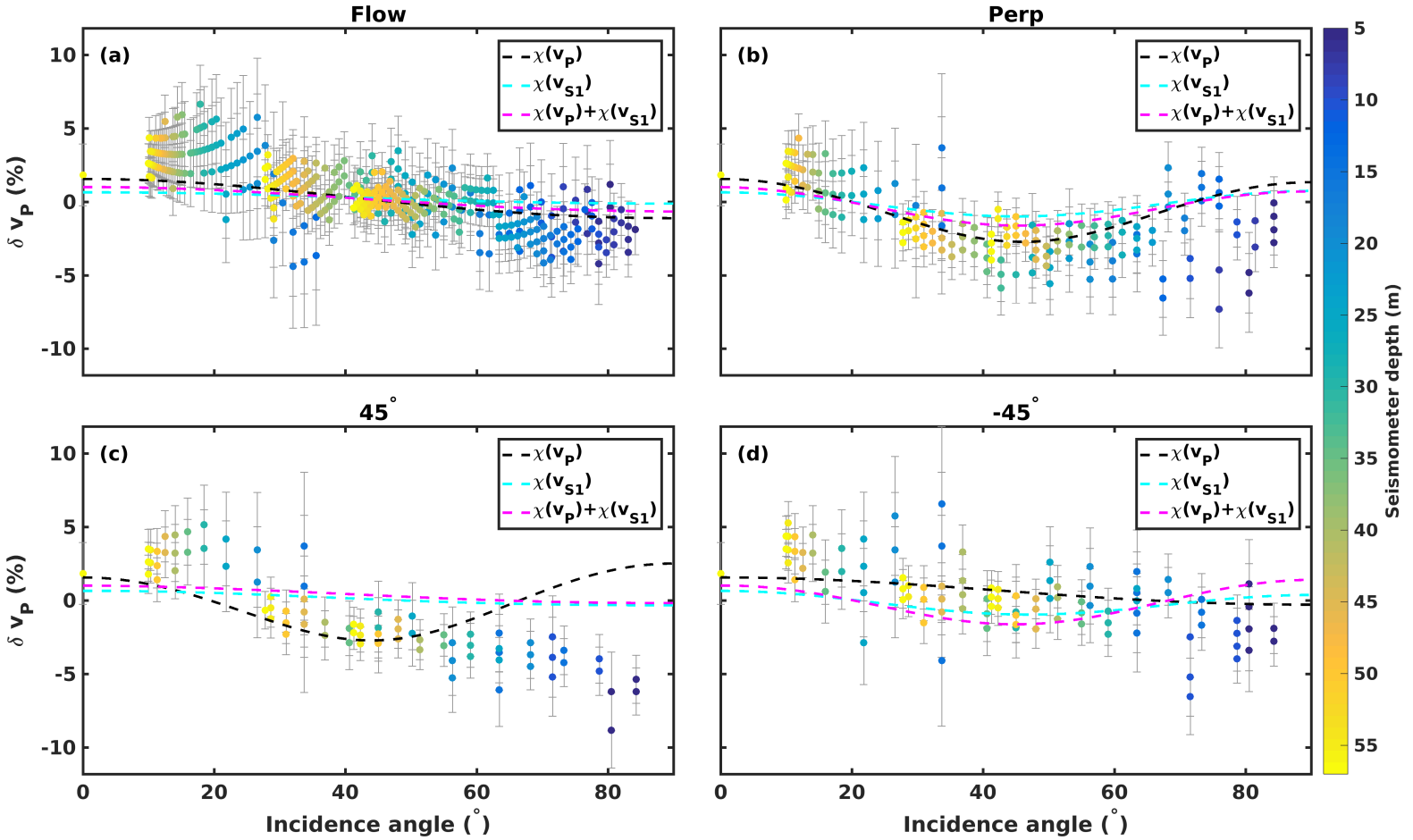

Figure 8. Multi-azimuth P-wave observed velocity anisotropy (symbols) and model results (dashed lines) along the different profiles. Symbol colour shows sensor depths. (a) Flow-profile (b) Perp-profile (c) $45°$-profile (d) $-45°$-profile

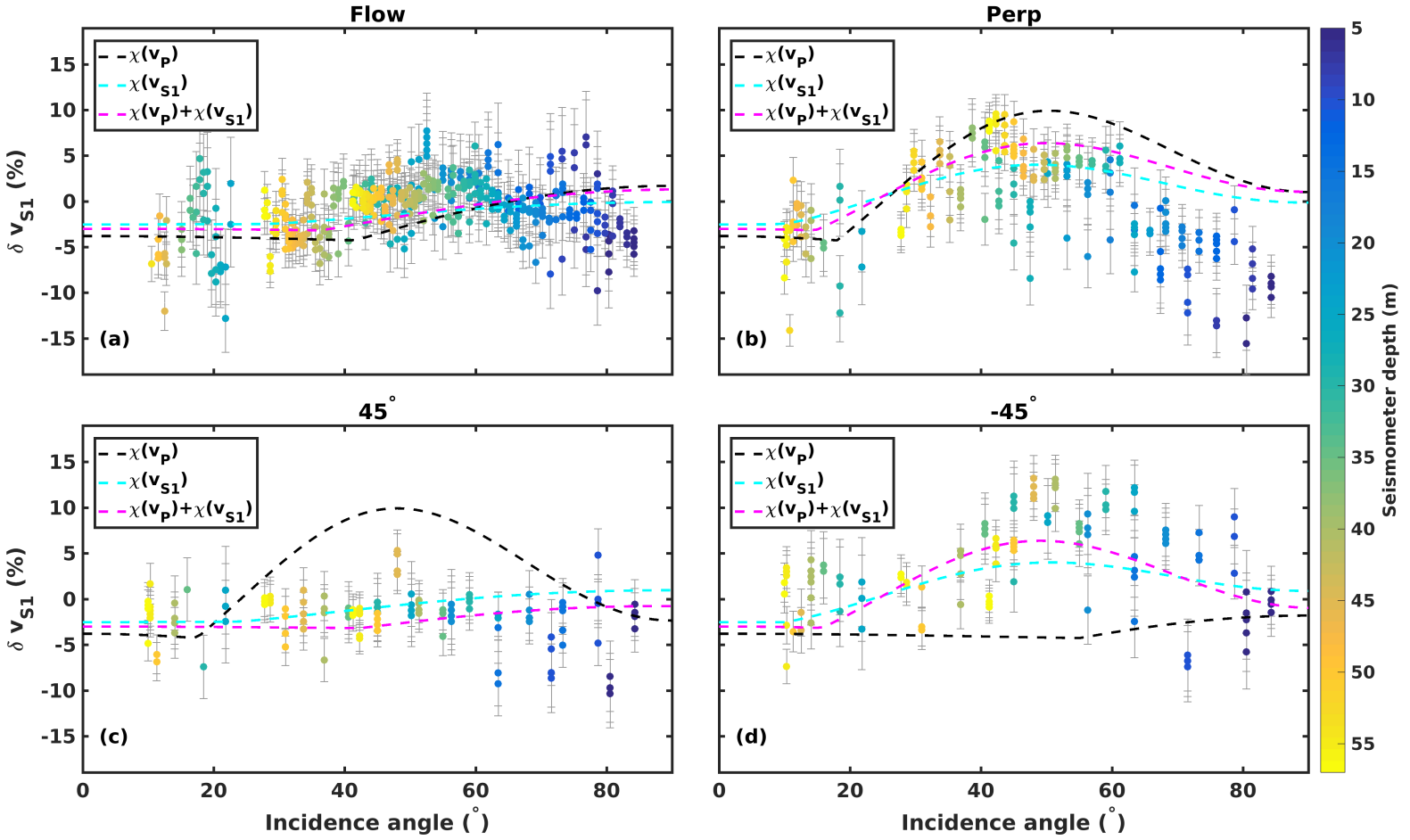

Figure 9. Multi-azimuth S-wave observed velocity anisotropy (symbols) and model results (dashed lines) along the different profiles. Symbol colour shows sensor depths. (a) Flow-profile (b) Perp-profile (c) $45°$-profile (d) $-45°$-profile

4.4 CPO model fit using ultrasonic velocities

Misfits χ of the Horizontal_Cluster_CPO are calculated from the multiazimuth observations of v_P, v_{S1} and v_{S2} on the core samples 003, 007 and 010.

Figure 10 shows misfits χ of the different velocities for sample 003, where the red mark indicates the best-fitting model. The individual misfits in Figures 10(a)-(c) and the sum of all misfits in Figure 10(d) show best-fitting models with a consistent cluster orientation and a small scatter in reconstructed cluster opening angles. The shape of the areas of lowest misfit shows that cluster orientation can be constrained with higher confidence than cluster width. An overview of CPO model parameters informed by the ultrasonic measurements is provided in Table 4. The misfit informed by v_{S1} in Figure 10(b) shows a ~~side~~local minimum at an orientation that is $\sim 90°$ offset from the best-fitting model. This reflects the shape of the measured v_{S1} variation with azimuth which shows an approximate $90°$ periodicity, whereas v_P and v_{S2} show $180°$ periodicity (see Figure 5). The sum of all misfits (Figure 10(d)) is regarded to provide the most reliable constraint on model fit. Here, the ~~side~~local minimum present in $\chi(v_{S1})$ is attenuated which resolves the ambiguity in the CPO model constraint.

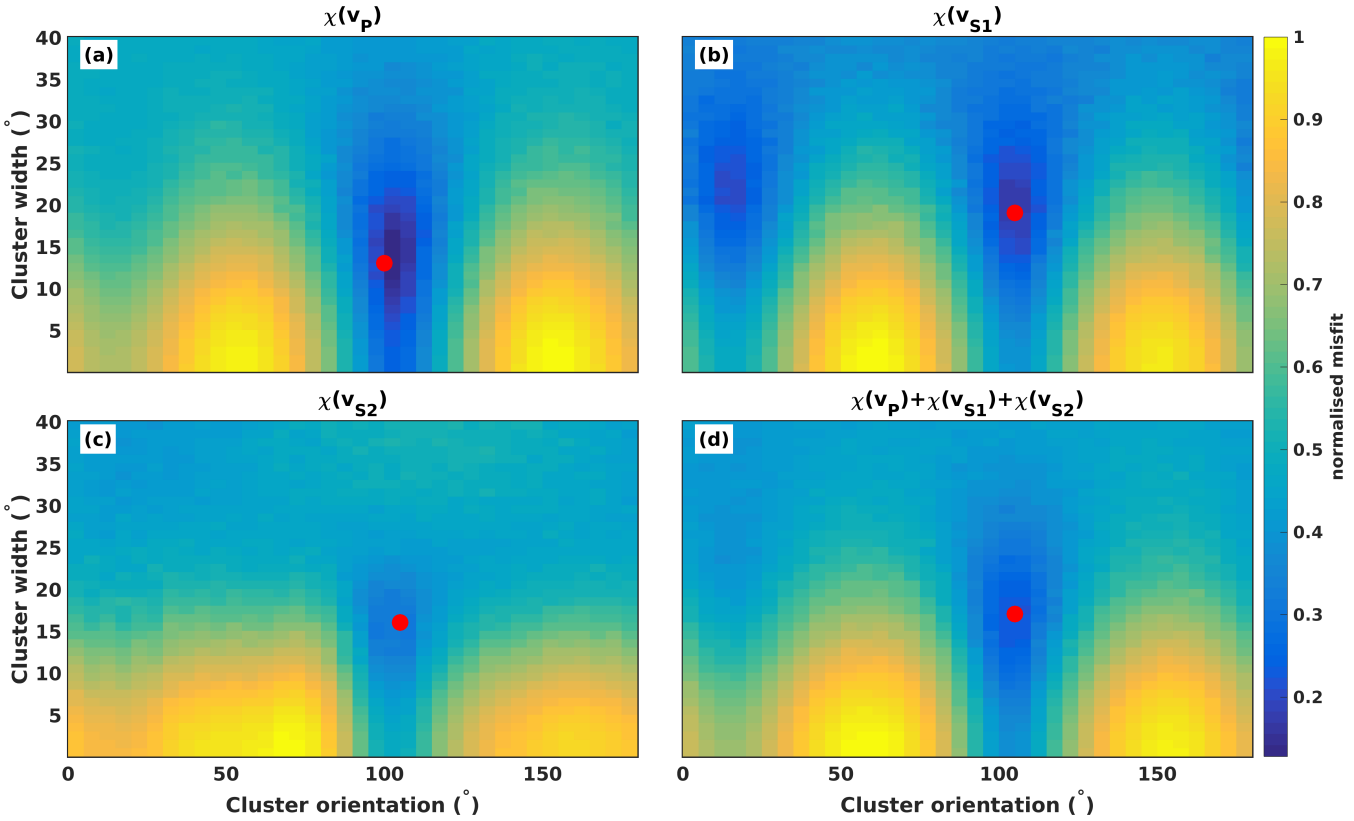

Figure 10. Misfit surfaces of seismic velocities showing fit to model parameters of the Horizontal_Cluster_CPO for sample 003: (a) $\chi(v_P)$ (b) $\chi(v_{S1})$ (c) $\chi(v_{S2})$ (d) $\chi(v_P) + \chi(v_{S1}) + \chi(v_{S2})$

Table 4. Best-fitting CPO model parameters and uncertainties informed by ultrasonic data.

Misfit type / sample	Cluster orientation φ (°)	Cluster width α (°)	Misfit
$\chi(v_P)$ (003)	100 [100,105]	13.1 [9.1,18.1]	0.13 [0.17]
$\chi(v_{S1})$ (003)	105 [100,105]	19.1 [16.1,23.1]	0.18 [0.20]
$\chi(v_{S2})$ (003)	105 [95,105]	16.1 [12.1,18.1]	0.31 [0.33]
$\sum\chi$ (003)	105 [100,105]	17.1 [13.1,20.1]	0.22 [0.24]
$\sum\chi$ (007)	125 [120,130]	14.1 [10.1,19.1]	0.16 [0.22]
$\sum\chi$ (010)	130 [125,135]	14.1 [8.1,18.1]	0.16 [0.22]

The best-fitting models of the three core samples are identified by the minimum in the misfit sum $\chi(v_P)+\chi(v_{S1})+\chi(v_{S2})$. The c-axes distribution of these CPO models are shown in upper hemisphere plots in Figure 11 alongside the measured CPO of the samples.

~~Measured and modelled CPO of sample 003 show excellent agreement, however for samples 007 and 010 the modelled CPO clusters are slightly rotated in clockwise direction relative to the measured CPO geometry. A comparison of observed and forward modelled velocity variations is given for sample 003 in Figure 12 which highlights that the constrained CPO model explains measured and CPO predicted seismic anisotropy to a high degree.~~

~~Observed and modelled velocity anisotropy for sample 007 are shown in Figure 13. Observed and modelled anisotropy are in excellent agreement, but both curves are clearly offset by $\sim 10^\circ$ from the predicted velocity variations from measured CPO in this sample.~~

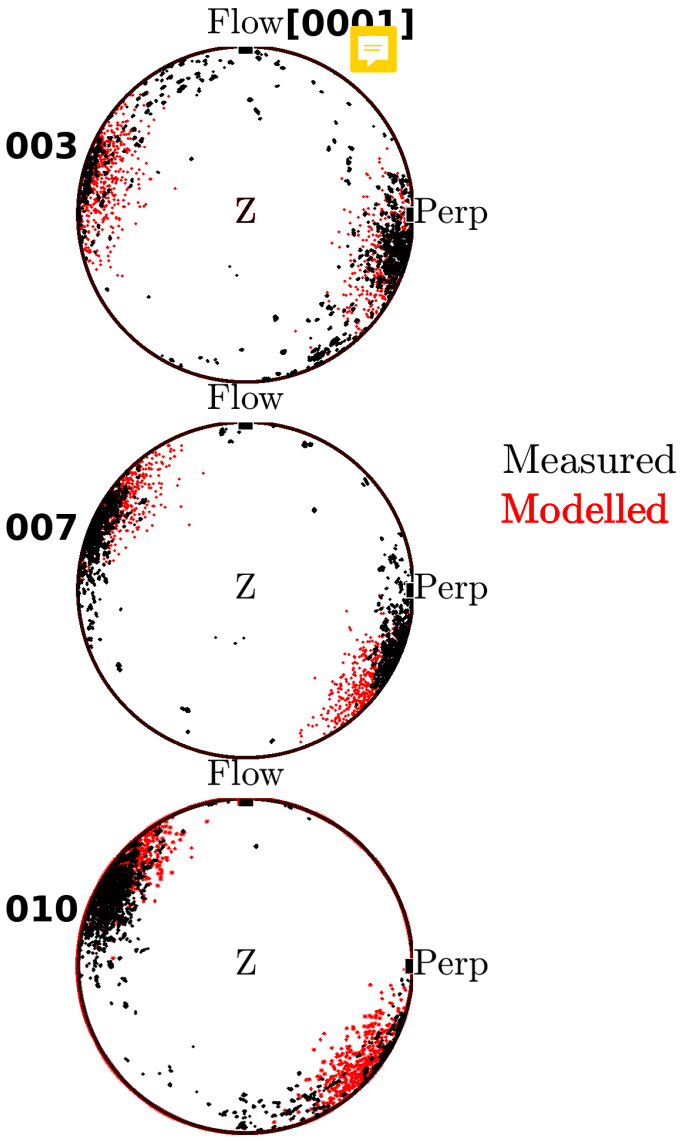

Figure 11. Measured (~~left~~black) and modelled (~~right~~red) CPO geometries. The VSP profile orientations of the "Flow" and "Perp" profiles are labelled. Top ~~row~~: sample 003, middle ~~row~~: sample 007, bottom ~~row~~: sample 010.

5 Discussion

5.1 Horizontal Cluster reconstruction

Both the VSP data and the ultrasonic data are best-matched by CPOs with cluster azimuths between 105° and 130° from the macroscopic ice flow direction at the site. This is consistent with CPO measurements made on core samples using EBSD analysis (Thomas et al., 2021). The agreement in model results between ultrasonic and seismic data bridges the two different scales at which these measurements are made. Ultrasonic and EBSD measurements that are made in ice core samples are shown to be representative of anisotropy within the macroscopic volume that is sampled by the VSP survey.

The inter-sample variation of CPO cluster orientations inside the shallow ice at the site (Thomas et al., 2021) is also clearly visible in the ultrasonic velocity variation: Figure 5 shows that the ultrasonic velocities in the three samples follow ~~highly~~ similar patterns, which are ~~however~~ slightly offset between the individual samples. Different fast seismic directions in the studied samples are apparent in Figure 5, especially between sample 003 and samples 007/010. Consequently the CPO model of 003 shows a different cluster azimuth than the models of samples 007 and 010 in Figure 11.

The c-axis maxima modelled from seismic anisotropies for samples 007 and 010 are rotated around the vertical axis relative to CPO measurements. Measured and modelled CPO of sample 003 show excellent agreement, however for samples 007 and 010 the modelled CPO clusters are slightly rotated in clockwise direction relative to the measured CPO geometry. A comparison of observed and forward modelled velocity variations is given for sample 003 in Figure 12 which highlights that the constrained CPO model explains measured and CPO predicted seismic anisotropy to a high degree.

Observed and modelled velocity anisotropy for sample 007 are shown in Figure 13. Observed and modelled anisotropy are in excellent agreement, but both curves are clearly offset by $\sim 10°$ from the predicted velocity variations from measured CPO in this sample. This azimuthal difference between measured and modelled CPOs is best explained by small scale variation within the samples. There is a potential azimuthal error of up to about 3° in cutting and mounting samples for CPO measurement, and this error will primarily be a rotation around the core axis. Probably more important is the fact that the locations of CPO and ultrasonic measurements for a sample do not coincide. As small-scale rotations of the c-axis maximum, around a vertical axis, are observed in the core (Thomas et al., 2021), a difference of a few ~~10s of mm~~centimetres in sample position could give a few degrees rotation of the c-axis maxima. Some sample locations, through the depth of the core, have a population of "oddly" oriented grains, in addition to a main c-axis maximum (Thomas et al., 2021), that would give rise to a rotation around a vertical axis of sample average acoustic anisotropy of $\sim 10°$: areas with and without this orientation population can occur within the same core section (Figure 9 in Thomas et al. (2021)).

The seismic VSP data records wavelengths that are larger than the scale of individual samples and therefore do not resolve a variation of cluster orientation at this scale. The CPO model informed by VSP velocities provides an averaging of any given variation in CPO properties over the entire sampled depth range. The CPO model found to best explain the VSP data is characterised by a slightly larger cone opening angle compared to results of the individual ultrasonic measurements and therefore exhibiting slightly weaker anisotropy.

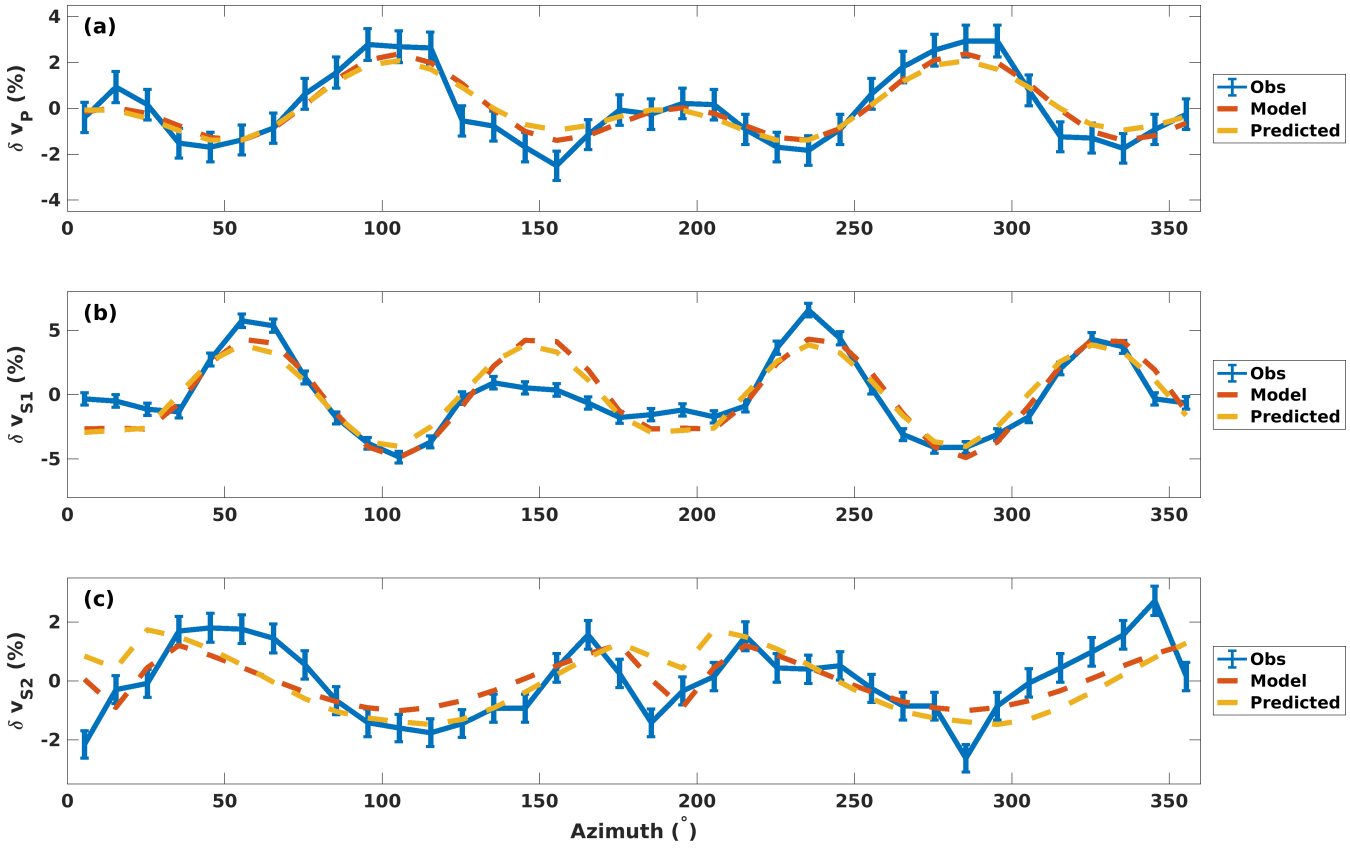

Figure 12. Observed, modelled and CPO-predicted anisotropy for sample 003. (a) δv_P (b) δv_{S1} (c) δv_{S2}

5.2 The role of studied seismic phase (P- or S-wave) and survey geometry on CPO model ambiguity

The VSP seismic and ultrasonic datasets presented in this study have fundamentally different acquisition geometries which ultimately determine the observed velocity variation due to CPO. The constraint of CPO models from seismic anisotropy is consequently highly sensitive to the sampling geometry.

The acquisition geometry of the VSP survey will have a critical control on the ability to distinguish different CPO patterns. For example the Flow and Perp lines show equally good P-wave (Figure 8a,b) and S-wave (Fig 9a,b) fits to the $\chi(v_p)$ model, which has the c-axis cluster azimuth at 65° (Figure 7a, Table 3) and to the $\chi(v_{S1})$ and $\sum\chi$ models, which have the c-axis cluster azimuths of 110° to 115° (Figure 7b,c, Table 3). The diagonal lines show clear differences in the predictions of the $\chi(v_p)$ model and the other models in both P-wave (Figure 8c,d) and S-wave (Figure 9c,d) velocity variations with incidence angle. Modelling CPOs based on P-wave traveltimes alone does not give a good fit to the EBSD data on diagonal lines: using S-wave traveltimes or S-waves traveltimes combined with P-wave traveltimes gives a much better fit to the EBSD measurements.

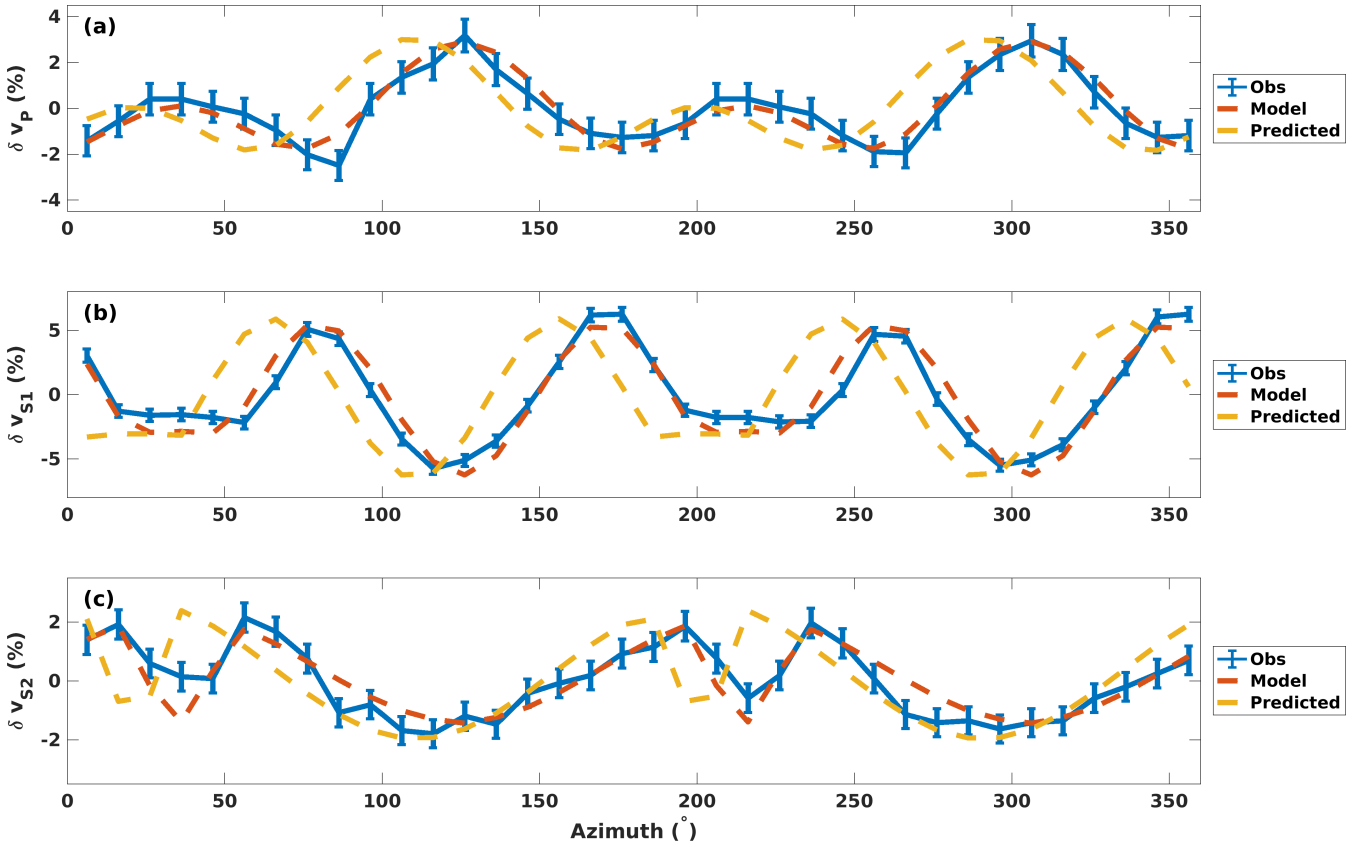

Figure 13. Observed, modelled and CPO-predicted anisotropy for sample 007. (a) δv_P (b) δv_{S1} (c) δv_{S2}

The ultrasonic data offer a dense sampling of velocities along azimuths in the horizontal direction. The given CPO type with horizontal c-axes clusters exhibits the largest magnitude of velocity variation in the horizontal plane, therefore this sampling geometry results in high sensitivity to CPO parameters. The individual reconstructed CPO models using either v_P, v_{S1} or v_{S2} anisotropy are found to be consistent and also generally agree with measured CPO in core samples (see Figures 10 and 11). Periodicity of seismic anisotropy can ~~however~~ result in ambiguities: δv_P and δv_{S2} exhibit $180°$ periodicity and reconstruct the CPO cluster's measured orientation without ambiguity. The cluster orientation reconstructed by $\chi(v_{S1})$ is also found to agree with measured orientation, however a misfit ~~side~~local minimum, offset by $90°$ azimuth to the global misfit minimum, reduces confidence in the results. We propose to consider the information from velocity measurements of all phases that are available to avoid a ~~side~~local minimum. In this study this is done by forming the sum of individual misfits χ and selecting the model associated with the misfit minimum in this case.

~~The usefulness of velocity information from different seismic phases becomes even more apparent in a sparse sampling geometry, which is simulated here by downsampling of the multiazimuth ultrasonic dataset.~~The influence of azimuthal sampling on model results is investigated by sub-sampling of the multiazimuth ultrasonic dataset to inform CPO models. Figure 14 presents model parameter results for sample 003

where, instead of 10° azimuth spacing between measurements, increments of 20°, 30°, 60° and 90° are used to inform CPO models. For each chosen new sampling interval, all possible downsampled datasets are considered. For example, an azimuth spacing of 20° allows two downsampled datasets to be created: one, where the first measurement is taken at 0° azimuth and another one, where the first measurement is at 10°.

Models informed by $\chi(v_P)$ (Figure 14(a)) confirm the result of the full dataset if a coarser sampling of velocities with azimuths increments 20°, 30° or 60° is chosen. Models informed by multiazimuth measurements with 90° spacing show a large spread of CPO parameter results. Models informed by $\chi(v_{S1})$ and $\chi(v_{S2})$ (Figures 14(b)~~+~~ and (c)) agree for spacings of 20° and 30°, with larger spacings resulting in a wide scatter of model parameters. At 60° sampling, $\chi(v_{S1})$ reconstructs three models at the realistic cluster orientation and three models at the 90° offset orientation associated with the misfit ~~side~~local minimum in Figure 10(b). The approach of using the sum of all misfits (Figure 14(d)) reduces the spread of found model parameters and finds realistic models for 20° and 30° spacing. For 60° spacing the cluster orientation angle is correctly found, however the cluster width poorly constrained. This is a clear improvement relative to the reconstructed model parameters in Figure 14(b)~~+~~ and (c) for 60° spacing. The results for 90° spacing are ~~however still largely~~widely scattered and ~~unrealistic~~not in agreement with the model parameters that were found using the full dataset. The discrepancy in model parameter results found by the different 90° sampling geometry relates to the fact that there is more than one cluster orientation that will give the same ratios of orthogonal velocities. Thus the solution is very dependent on the measurement errors in the velocity data set. At 90° sampling the errors in v_{S1} will be particularly influential as v_{S1} velocities should be very similar for orthogonal azimuths (see predictions in Figures 12 and 13).

Our downsampling analysis shows that an ideal survey geometry, which is in this case given by the sampling of a Horizontal-Cluster-CPO by horizontal velocity measurements, a realistic CPO model can be created from sampling in up to 30° steps regardless of the studied seismic phase. Observed scatter in model parameter results shows that ~~aliasing~~the set of actual sampled azimuths becomes ~~a~~ critical ~~effect~~ for larger sampling intervals: the datasets with 20° and 30° sampling are much less sensitive to the choice of first sampled azimuth compared to the datasets with 60° and 90° spacing. The consideration of the full range of seismic velocity information ($\chi(v_P) + \chi(v_{S1}) + \chi(v_{S2})$) can reduce scatter and aid to reconstruct a realistic CPO model from ~~coarsely sampled data~~data with a wider azimuthal spacing.

The VSP survey CPO modelling presents ambiguity in cluster orientation if only P-wave velocities are considered, as shown in Figure 7(a). The best-fitting model in this case does not match the CPO observations from the site, orienting the cluster at an azimuth that is offset by $\sim 45°$ in anticlockwise direction from observed cluster orientations. The uncertainties in v_P measurements are generally larger than the P-wave anisotropy.

The difficulty to reconstruct a realistic CPO model from P-wave velocities in the VSP dataset is a consequence of poor azimuthal sampling. For the given CPO, the additional coverage of raypaths from a range of incidence angles provides little added sensitivity compared to a dense azimuthal sampling of horizontal velocities, which characterises the ultrasonic measurements. The inclusion of P- and S-wave phase information mitigates this shortcoming of the VSP data by resolving the ambiguity in cluster orientation and identifying a CPO model which is in agreement with measured CPO. The study of all available seismic

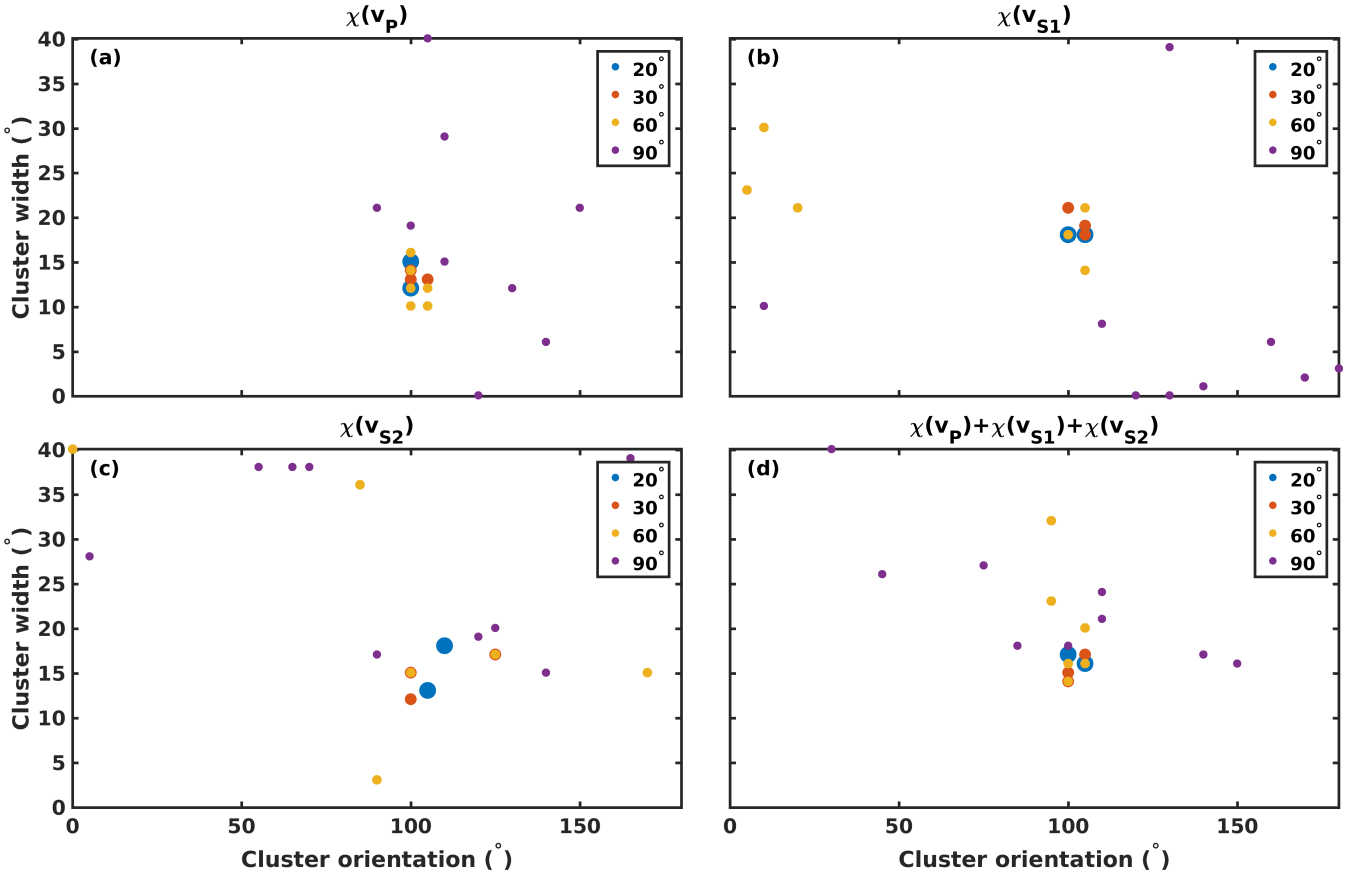

Figure 14. Parameter results using downsampled velocity measurements with azimuthal spacing of 20°, 30°, 60° and 90° (indicated by symbol size) for sample 003: (a) $\chi(v_P)$ (b) $\chi(v_{S1})$ (c) $\chi(v_{S2})$ (d) $\chi(v_P) + \chi(v_{S1}) + \chi(v_{S2})$

phases should therefore become standard in seismic CPO constraints in ice, rather than the commonly encountered focus on P-wave velocities.

For the Horizontal-Cluster-CPO, the variation of seismic velocities with incidence angle is highly dependent on the azimuth. Therefore, VSP data might be unable to constrain this CPO if azimuths with strong variation are not sampled. The difficulty to find a correct CPO model from VSP P-wave velocities could be a consequence of this problem, highlighted in Figure 8 by large errorbars relative to the overall v_P variation with incidence angle. ~~The survey design could be improved by sampling of more profiles in finer azimuth spacing to increase confidence in the determined models~~A greater azimuthal sampling of VSP data is required to improve the CPO model constraint. Furthermore, larger shot offsets should be targeted to sample near-horizontal raypaths for the study of Horizontal-Cluster-CPOs, since the largest amplitude of the anisotropy signal is in the horizontal plane.

6 Conclusions

We have conducted a vertical-seismic-profile (VSP) experiment and laboratory ultrasonic experiments aimed at measuring the seismic anisotropy of ice from the lateral shear margin of the Priestley Glacier, Antarctica, and linking these data to seismic anisotropy model predictions based on measured crystallographic preferred orientations (CPOs) in EBSD data.

P-wave and S-wave velocity anisotropy data from a ~ 50 m-scale, four-azimuth, walkaway-VSP experiment ~~matches~~agree with predictions from the horizontally clustered ice c-axes measured in the ice core from the borehole used for the VSP experiment. A CPO model informed by P-wave data alone gives two equally likely orientations of the c-axis maximum azimuth, one of which is correct~~, and~~. Using P-wave data alone overestimates the strength of c-axes clustering. S-wave data alone or P-wave and S-wave data combined give a unique model best-fit that ~~matches~~agrees with c-axis measurements.

Azimuthal ultrasonic P-wave and S-wave velocity measurements, made in 10° increments, on core samples from the borehole show the pattern of anisotropy with considerable detail. The anisotropy pattern matches the pattern predicted from the CPO in the same sample. The anisotropy patterns in different samples are rotated through small angles relative to each other around the core axis: a pattern that matches direct CPO measurements.

The ultrasonic data have been ~~degraded~~downsampled to larger azimuthal increments (20°, 30°, 60° and 90°) to explore how well these lower resolution data constrain the CPO responsible for velocity anisotropy. Increments of up to 30° constrain both the azimuthal orientation and intensity of horizontal c-axis alignment well. 60° increments constrain orientation. 90° increments do not provide useful constraints. The design of field seismic surveys should be designed to address ambiguity as result of aliasing by considering two main points. First, a dense sampling of propagation angles must be realised by the acquisition geometry. Second, sources and receivers must enable to derive both P-wave and S-wave anisotropy.

Data availability. VSP seismic data, ultrasonic data and traveltime picks are available at https://figshare.com/s/8effdc8b145d79fc1788 (Lutz et al., 2021).

Author contributions. DJP and CLH lead the Priestley Glacier project. DJP and FL designed the seismic and ultrasonic experiments. FL collected the bulk of the ultrasonic data. HS collected the axial ultrasonic data. SF wrote MTEX code used to simulate CPOs. All authors except CLH and SF were involved in seismic data collection in the field. FL wrote the manuscript in collaboration with DJP. All authors edited the manuscript.

Competing interests. The authors declare that there are no competing interests present.

Acknowledgements. We would like to acknowledge the logistics support from Antartica New Zealand and field support from from staff at Scott Base, Mario Zucchelli and Jang Bogo research stations. We would also like to thank Brent Pooley for building the ultrasonic rig. Funding for this research was provided by the Royal Society of New Zealand Marsden Fund grant UOO1716 "Stretching ice to the limit: New flow laws for ice sheet modelling" and Korea Polar Research Institute project PE22430. FL is funded by a NZARI Early Career Researcher Seed Grant.

References

Azuma, N. and Goto-Azuma, K.: An anisotropic flow law for ice-sheet ice and its implications, Annals of Glaciology, 23, 202–208, https://doi.org/10.3189/S0260305500013458, 1996.

Bentley, C. R.: Seismic Anisotropy in the West Antarctic Ice Sheet, pp. 131–177, American Geophysical Union, https://doi.org/10.1029/AR016p0131, 1971.

Blankenship, D. D. and Bentley, C. R.: The crystalline fabric of polar ice sheets inferred from seismic anisotropy, The Physical Basis of Ice Sheet Modelling, 70, 17–28, 1987.

Bouchez, J. and Duval, P.: The fabric of polycrystalline ice deformed in simple shear: experiments in torsion, natural deformation and geometrical interpretation, Texture, Stress, and Microstructure, 5, 171–190, 1982.

Budd, W. F., Warner, R. C., Jacka, T., Li, J., and Treverrow, A.: Ice flow relations for stress and strain-rate components from combined shear and compression laboratory experiments, Journal of Glaciology, 59, 374–392, https://doi.org/10.3189/2013JoG12J106, 2013.

Diez, A. and Eisen, O.: Seismic wave propagation in anisotropic ice-Part 1: Elasticity tensor and derived quantities from ice-core properties, The Cryosphere, 9, 367–384, 2015.

Diez, A., Eisen, O., Hofstede, C., Lambrecht, A., Mayer, C., Miller, H., Steinhage, D., Binder, T., and Weikusat, I.: Seismic wave propagation in anisotropic ice–Part 2: Effects of crystal anisotropy in geophysical data, The Cryosphere, 9, 385–398, 2015.

Drews, R., Wild, C. T., Marsh, O. J., Rack, W., Ehlers, T. A., Neckel, N., and Helm, V.: Grounding-Zone Flow Variability of Priestley Glacier, Antarctica, in a Diurnal Tidal Regime, Geophysical Research Letters, 48, e2021GL093 853, https://doi.org/https://doi.org/10.1029/2021GL093853, 2021.

Ershadi, M. R., Drews, R., Martín, C., Eisen, O., Ritz, C., Corr, H., Christmann, J., Zeising, O., Humbert, A., and Mulvaney, R.: Polarimetric radar reveals the spatial distribution of ice fabric at domes in East Antarctica, The Cryosphere Discussions, 2021, 1–34, https://doi.org/10.5194/tc-2020-370, 2021.

Faria, S. H., Weikusat, I., and Azuma, N.: The microstructure of polar ice. Part I: Highlights from ice core research, Journal of Structural Geology, 61, 2 – 20, https://doi.org/https://doi.org/10.1016/j.jsg.2013.09.010, microdynamics of Ice, 2014.

Frezzotti, M., Tabacco, I. E., and Zirizzotti, A.: Ice discharge of eastern Dome C drainage area, Antarctica, determined from airborne radar survey and satellite image analysis, Journal of Glaciology, 46, 253–264, https://doi.org/10.3189/172756500781832855, 2000.

Gammon, P. H., Kiefte, H., Clouter, M. J., and Denner, W. W.: Elastic Constants of Artificial and Natural Ice Samples by Brillouin Spectroscopy, Journal of Glaciology, 29, 433–460, https://doi.org/10.3189/S0022143000030355, 1983.

Gerbi, C., Mills, S., Clavette, R., Campbell, S., Bernsen, S., Clemens-Sewall, D., Lee, I., Hawley, R., Kreutz, K., Hruby, K., and et al.: Microstructures in a shear margin: Jarvis Glacier, Alaska, Journal of Glaciology, p. 1–14, https://doi.org/10.1017/jog.2021.62, 2021.

Gusmeroli, A., Murray, T., Clark, R. A., Kulessa, B., and Jansson, P.: Vertical seismic profiling of glaciers: Appraising multi-phase mixing models, Annals of Glaciology, 54, 115–123, 2013.

Hellmann, S., Grab, M., Kerch, J., Löwe, H., Bauder, A., Weikusat, I., and Maurer, H.: Acoustic velocity measurements for detecting the crystal orientation fabrics of a temperate ice core, The Cryosphere, 15, 3507–3521, https://doi.org/10.5194/tc-15-3507-2021, 2021.

Hill, R.: The Elastic Behaviour of a Crystalline Aggregate, Proceedings of the Physical Society. Section A, 65, 349, http://stacks.iop.org/0370-1298/65/i=5/a=307, 1952.

Hruby, K., Gerbi, C., Koons, P., Campbell, S., Martín, C., and Hawley, R.: The impact of temperature and crystal orientation fabric on the dynamics of mountain glaciers and ice streams, Journal of Glaciology, 66, 755–765, https://doi.org/10.1017/jog.2020.44, 2020.

Hudleston, P. J.: Structures and fabrics in glacial ice: A review, Journal of Structural Geology, 81, 1 – 27, https://doi.org/https://doi.org/10.1016/j.jsg.2015.09.003, 2015.

Jackson, M. and Kamb, B.: The marginal shear stress of Ice Stream B, West Antarctica, Journal of Glaciology, 43, 415–426, https://doi.org/10.3189/S0022143000035000, 1997.

Jordan, T., Schroeder, D., Elsworth, C., and Siegfried, M.: Estimation of ice fabric within Whillans Ice Stream using polarimetric phase-sensitive radar sounding, Annals of Glaciology, https://doi.org/10.1017/aog.2020.6, 2020.

Journaux, B., Chauve, T., Montagnat, M., Tommasi, A., Barou, F., Mainprice, D., and Gest, L.: Recrystallization processes, microstructure and crystallographic preferred orientation evolution in polycrystalline ice during high-temperature simple shear, The Cryosphere, 13, 1495–1511, https://doi.org/10.5194/tc-13-1495-2019, 2019.

Langway, C., Shoji, H., and Azuma, N.: Crystal Size and Orientation Patterns in the Wisconsin-Age Ice from Dye 3, Greenland, Annals of Glaciology, 10, 109–115, https://doi.org/10.3189/S0260305500004262, 1988.

LeDoux, C. M., Hulbe, C. L., Forbes, M. P., Scambos, T. A., and Alley, K.: Structural provinces of the Ross Ice Shelf, Antarctica, Annals of Glaciology, p. 1–11, https://doi.org/10.1017/aog.2017.24, 2017.

Lilien, D. A., Rathmann, N. M., Hvidberg, C. S., and Dahl-Jensen, D.: Modeling Ice-Crystal Fabric as a Proxy for Ice-Stream Stability, Journal of Geophysical Research: Earth Surface, 126, e2021JF006 306, https://doi.org/https://doi.org/10.1029/2021JF006306, e2021JF006306 2021JF006306, 2021.

Lutz, F., Eccles, J., Prior, D. J., Craw, L., Fan, S., Hulbe, C., Forbes, M., Still, H., Pyne, A., and Mandeno, D.: Constraining Ice Shelf Anisotropy Using Shear Wave Splitting Measurements from Active-Source Borehole Seismics, Journal of Geophysical Research: Earth Surface, 125, e2020JF005 707, https://doi.org/10.1029/2020JF005707, e2020JF005707 10.1029/2020JF005707, 2020.

Lutz, F., Prior, D. J., Still, H., Bowman, M. H., Boucinhas, B., Craw, L., Fan, S., Kim, D., Mulvaney, R., Thomas, R. E., and Hulbe, C. L.: Priestley Glacier seismic and ultrasonic datasets, https://doi.org/10.17608/k6.auckland.17108639, 2021.

Mainprice, D.: Seismic Anisotropy of the Deep Earth from a Mineral and Rock Physics Perspective, vol. 2, pp. 437–492, https://doi.org/10.1016/B978-044452748-6/00045-6, 2007.

Mainprice, D., Hielscher, R., and Schaeben, H.: Calculating anisotropic physical properties from texture data using the MTEX open-source package, Geological Society, London, Special Publications, 360, 175–192, https://doi.org/10.1144/SP360.10, 2011.

Matsuoka, K., Furukawa, T., Fujita, S., Maeno, H., Uratsuka, S., Naruse, R., and Watanabe, O.: Crystal orientation fabrics within the Antarctic ice sheet revealed by a multipolarization plane and dual-frequency radar survey, Journal of Geophysical Research: Solid Earth, 108, https://doi.org/https://doi.org/10.1029/2003JB002425, 2003.

Maurel, A., Lund, F., and Montagnat, M.: Propagation of elastic waves through textured polycrystals: application to ice, Proceedings of the Royal Society of London A: Mathematical, Physical and Engineering Sciences, 471, https://doi.org/10.1098/rspa.2014.0988, 2015.

Minchew, B. M., Meyer, C. R., Robel, A. A., Gudmundsson, G. H., and Simons, M.: Processes controlling the downstream evolution of ice rheology in glacier shear margins: case study on Rutford Ice Stream, West Antarctica, Journal of Glaciology, 64, 583–594, https://doi.org/10.1017/jog.2018.47, 2018.

Monz, M. E., Hudleston, P. J., Prior, D. J., Michels, Z., Fan, S., Negrini, M., Langhorne, P. J., and Qi, C.: Full crystallographic orientation (c and a axes) of warm, coarse-grained ice in a shear-dominated setting: a case study, Storglaciären, Sweden, The Cryosphere, 15, 303–324, https://doi.org/10.5194/tc-15-303-2021, 2021.

Mouginot, J., Rignot, E., and Scheuchl, B.: Continent-Wide, Interferometric SAR Phase, Mapping of Antarctic Ice Velocity, Geophysical Research Letters, 46, 9710–9718, https://doi.org/10.1029/2019GL083826, 2019.

Picotti, S., Vuan, A., Carcione, J. M., Horgan, H. J., and Anandakrishnan, S.: Anisotropy and crystalline fabric of Whillans Ice Stream (West Antarctica) inferred from multicomponent seismic data, Journal of Geophysical Research: Solid Earth, 120, 4237–4262, 2015.

Qi, C., Prior, D. J., Craw, L., Fan, S., Llorens, M.-G., Griera, A., Negrini, M., Bons, P. D., and Goldsby, D. L.: Crystallographic preferred orientations of ice deformed in direct-shear experiments at low temperatures, The Cryosphere, 13, 351–371, https://doi.org/10.5194/tc-13-351-2019, 2019.

Sayers, C. M.: Increasing contribution of grain boundary compliance to polycrystalline ice elasticity as temperature increases, Journal of Glaciology, 64, 669–674, https://doi.org/10.1017/jog.2018.56, 2018.

Still, H., Hulbe, C., Forbes, M., Prior, D. J., Bowman, M. H., Boucinhas, B., Craw, L., Kim, D., Lutz, F., Mulvaney, R., and Thomas, R. E.: Tidal modulation of a lateral shear margin: Priestley Glacier, Antarctica, Frontiers in Earth Science: Cryospheric Sciences, https://doi.org/10.3389/feart.2022.828313, 2022.

Thomas, R. E., Negrini, M., Prior, D. J., Mulvaney, R., Still, H., Bowman, M. H., Craw, L., Fan, S., Hubbard, B., Hulbe, C., Kim, D., and Lutz, F.: Microstructure and Crystallographic Preferred Orientations of an Azimuthally Oriented Ice Core from a Lateral Shear Margin: Priestley Glacier, Antarctica, Frontiers in Earth Science, 9, 1084, https://doi.org/10.3389/feart.2021.702213, 2021.

Truffer, M. and Echelmeyer, K. A.: Of isbræ and ice streams, Annals of Glaciology, 36, 66–72, https://doi.org/10.3189/172756403781816347, 2003.

Vélez, J. A., Tsoflias, G. P., Black, R. A., van der Veen, C. J., and Anandakrishnan, S.: Distribution of preferred ice crystal orientation determined from seismic anisotropy: Evidence from Jakobshavn Isbræ and the North Greenland Eemian Ice Drilling facility, Greenland, Geophysics, 81, 111–118, https://doi.org/10.1190/geo2015-0154.1, 2016.

Wüstefeld, A., Al-Harrasi, O., Verdon, J. P., Wookey, J., and Kendall, J. M.: A strategy for automated analysis of passive microseismic data to image seismic anisotropy and fracture characteristics, Geophysical Prospecting, 58, 755–773, https://doi.org/10.1111/j.1365-2478.2010.00891.x, 2010.